

# A synthetic signalling network imitating the action of immune cells in response to bacterial metabolism

Michal Walczak,<sup>1</sup> Leonardo Mancini,<sup>1</sup> Jiayi Xu,<sup>1,2</sup> Federica Raguseo,<sup>3,4</sup>  
Jurij Kotar,<sup>1</sup> Pietro Cicuta,<sup>1</sup> and Lorenzo Di Michele<sup>2,3,4,1,\*</sup>

<sup>1</sup>*Biological and Soft Systems, Cavendish Laboratory,  
University of Cambridge, Cambridge, United Kingdom*

<sup>2</sup>*Department of Chemical Engineering and Biotechnology,  
University of Cambridge, Cambridge, United Kingdom*

<sup>3</sup>*Department of Chemistry, Molecular Sciences Research Hub,  
Imperial College London, London, United Kingdom*

<sup>4</sup>*fabriCELL, Molecular Sciences Research Hub, Imperial College London, London, United Kingdom*

(Dated: April 16, 2023)

State-of-the-art bottom-up synthetic biology allows us to replicate many basic biological functions in artificial cell-like devices. To mimic more complex behaviours, however, *artificial cells* would need to perform many of these functions in a synergistic and coordinated fashion, which remains elusive. Here we considered a sophisticated biological response, namely the capture and deactivation of pathogens by neutrophil immune cells, through the process of netosis. We designed a consortium consisting of two synthetic agents – responsive DNA-based particles and antibiotic-loaded lipid vesicles – whose coordinated action mimics the sought immune-like response when triggered by bacterial metabolism. The artificial netosis-like response emerges from a series of interlinked sensing and communication pathways between the live and synthetic agents, and translates into both physical and chemical antimicrobial actions, namely bacteria immobilisation and exposure to antibiotics. Our results demonstrate how advanced life-like responses can be prescribed with a relatively small number of synthetic molecular components, and outlines a new strategy for artificial-cell-based antimicrobial solutions.

## INTRODUCTION

Recent years have witnessed a substantial growth in the fields of artificial cell science and bottom-up synthetic biology [1–6], which aim at producing cell mimics capable of replicating the behaviours of biological cells. *Artificial cells* hold applicative potential in diagnostics [7] and therapeutics [8–11], as well as in fundamental biology and [12] origin of life research [13]. This interest has led to a rapid expansion of the available design toolkit for artificial cells, enabling replication of biological processes and features such as division [14–16], metabolism [17, 18], growth [19], motility [20, 21], communication [22, 23], sensing [24, 25], compartmentalisation [26–28], protein expression [29] and DNA replication [30]. Artificial cells have been successfully built from membrane-bound scaffolds in the form of liposomes [31, 32], polymericosomes [31, 33] and proteinosomes [34, 35], as well as from membrane-less coacervates or hydrogels [27, 36–39].

While these early successes in mimicking individual biological functions carry both applicative and fundamental interest, challenges remain in place when attempting to design artificial cells capable of sustaining more advanced biomimetic responses, where many elementary functions need to be performed in a coordinated way. Among the advanced behaviours we seek to implement are those that resemble the action of the immune system [40, 41], which would unlock disruptive applications of artificial cells to *in vivo* therapeutics [42].

In this scenario, artificial cells would need to establish multi-agent signalling and signal transduction networks with biological and other artificial cells, involving several interlinked responses: *i*) Detection and transduction of signals generated by live cells; *ii*) Communication with live cells and possibly other artificial cells; *iii*) Information processing; *iv*) Individual and/or collective responses that may involve both physical and chemical action, *e.g.* the release of therapeutic agents and the mechanical perturbation of live cells.

Successful attempts at establishing signalling networks between live and artificial cells have been reported, often involving one-way communication, *e.g.* triggering of bacterial gene expression [43–50], and more rarely two-way pathways leading to cell death [10]. However, these remarkable examples are still relatively simple, relying on one or a small number of individual functionalities, and thus failing to address the need to engineer more advanced emerging behaviours.

In this contribution, we aim to build a synthetic signalling network that mimics a complex response of the innate immune system, namely that of *netosis* [51–53], whereby neutrophils excrete a sticky *Neutrophil Extracellular Trap* (NET) formed from their genomic DNA, which traps pathogens and then disrupts them thanks to embedded antimicrobial proteins (Fig. 1a). As sketched in Fig. 1b, the synthetic pathway we propose features two artificial cell-like agents, *i*) responsive DNA-based

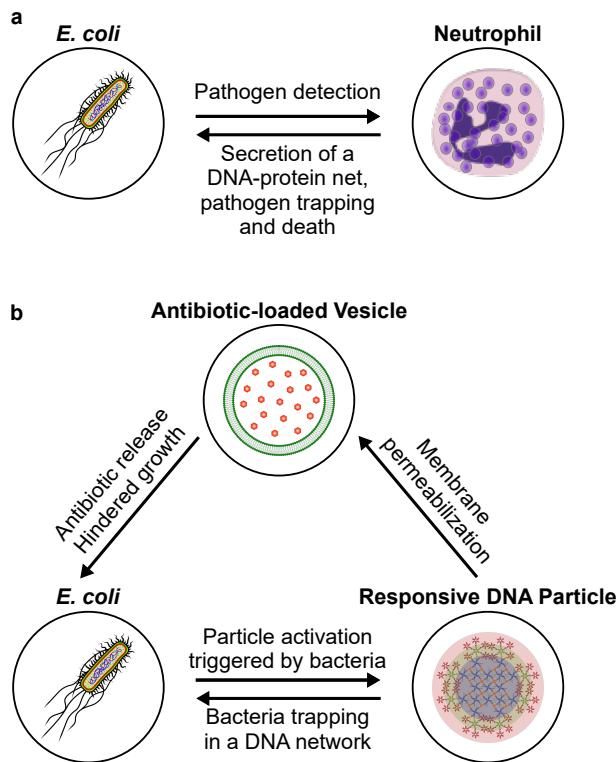


**FIG. 1. Three-agent synthetic consortium mimics the antimicrobial response of innate immune cells.** **a.** Neutrophils respond to the presence of pathogens by excreting a mesh formed by their genomic DNA, histones, and granules containing molecules with antimicrobial properties. The Neutrophil Extracellular Trap (NET) immobilises the pathogens and kills them due to the antimicrobial properties of the molecules associated. **b.** Three-agent synthetic consortium designed to exhibit a netosis-like response. Responsive DNA-based particles detect model targets (*E. coli*) by sensing medium acidification induced by the glucose metabolism of the cells. “Activated” particles respond by forming a sticky DNA-cholesterol network that immobilises the bacteria and, at the same time, permeabilises antibiotic-loaded Giant Unilamellar Vesicles (GUVs). Antibiotic release suppresses bacterial growth and division, fulfilling the antimicrobial role of the DNA-binding proteins in the biological system.

19 small number of molecular and nanoscale components. In  
20 addition, the platform represents a starting point for the  
21 development of biomimetic antimicrobial solutions and,  
22 more generally, synthetic-cell therapeutics.

## 23 RESULTS

### 24 Fabrication of pH-responsive DNA particles

25 Figure 2a shows the DNA-based particles used in  
26 this work, which feature a core-shell structure with  
27 an hydrophobised centre surrounded by an hydrophilic  
28 outer layer, the latter ensuring colloidal stability. The  
29 amphiphilic *core motifs* (CM) consist of 4-pointed  
30 DNA junctions (nanostars), with the end of each  
31 double-stranded (ds) DNA arm labelled by a cholesterol  
32 moiety. Similar “C-star” designs have been shown  
33 to self-assemble into framework-like materials sus-  
34 tained by cholesterol-mediated hydrophobic forces, with  
35 programmable nanoscale morphology and multi-stimuli-  
36 responsiveness [27, 54, 61–63]. The shell comprises of two  
37 6-pointed all-DNA nanostars, labelled as *inner* and *outer*  
38 *corona motifs* (ICM and OCM, respectively), together  
39 forming dendrimeric construct that can connect to core  
40 motifs through single-stranded (ss) DNA overhangs  
41 (Fig. 2a). As we recently demonstrated, the core-shell  
42 particle morphology can be attained following a two-step  
43 thermal annealing process, which can be adapted to  
44 prescribe the size of the particles, from a few hundred  
45 nanometres to several microns [54]. Figure 2b shows  
46 a large particle where the sought core-shell structure  
47 is clearly visible in confocal microscopy. Particles of  
48 this large size were purposefully created with a modified  
49 assembly protocol to enable facile confocal visualisa-  
50 tion. For the remainder of this work, the assembly  
51 protocol was set up to produce smaller particles, with  
52 hydrodynamic radius of either  $\sim 1\ \mu\text{m}$ ,  $\sim 750\ \text{nm}$ , or  
53  $\sim 200\ \text{nm}$ , depending on the specific experiment. Details  
54 of sample preparation are provided in the Methods, while  
55 sequences of all oligonucleotides used in the work and  
56 composition of all samples are shown in Supplementary  
57 Tables 1 and 2, respectively. Correct assembly of the  
58 individual core and corona motifs was verified with both  
59 Agarose Gel Electrophoresis (AGE) and Dynamic Light  
60 Scattering (DLS), summarised in Supplementary Figs 1  
61 and 2, while their thermal stability was assessed with  
62 UV-absorbance (Supplementary Fig. 3). In our previous  
63 contribution, we have demonstrated that removal of the  
64 corona, induced by a non-biologically-relevant ssDNA  
65 trigger, leads to exposure of the particles’ hydropho-  
66 bic cores and formation of a sticky DNA-cholesterol  
67 network [54]. The network has then been shown to  
68 trap motile *E. coli* and, independently, disrupt Giant  
69 Unilamellar lipid Vesicles (GUVs) [54]. These are two  
70 key functionalities for the netosis-like signalling network

1 particles [54] and *ii*) antibiotic-loaded liposomes, whose  
2 coordinated action, triggered by bacterial activity, gives  
3 rise to the sought behaviour. The DNA-particles sense  
4 a decrease in pH resulting from the natural glucose  
5 metabolism of *E. coli* [55], and respond by exposing their  
6 hydrophobic core, which then leads to the formation of  
7 a *synthetic DNA NET*. The sticky material traps and  
8 immobilises the bacteria and, at the same time, perme-  
9 abilises the liposomes, which ultimately release an  
10 antibiotic able to hinder growth of the trapped cells. The  
11 synthetic netosis pathway coordinates several function-  
12 alities, including one-way (particles  $\rightarrow$  liposomes and li-  
13 posomes  $\rightarrow$  bacteria) and two-way (particles  $\leftrightarrow$  bacte-  
14 ria) communication, a collective self-assembly response,  
15 and both physical and chemical interference with bacte-  
16 rial activity. Our proof-of-concept implementation thus  
17 demonstrates how advanced life-like behaviours can be  
18 engineered from the bottom-up, relying on a relatively

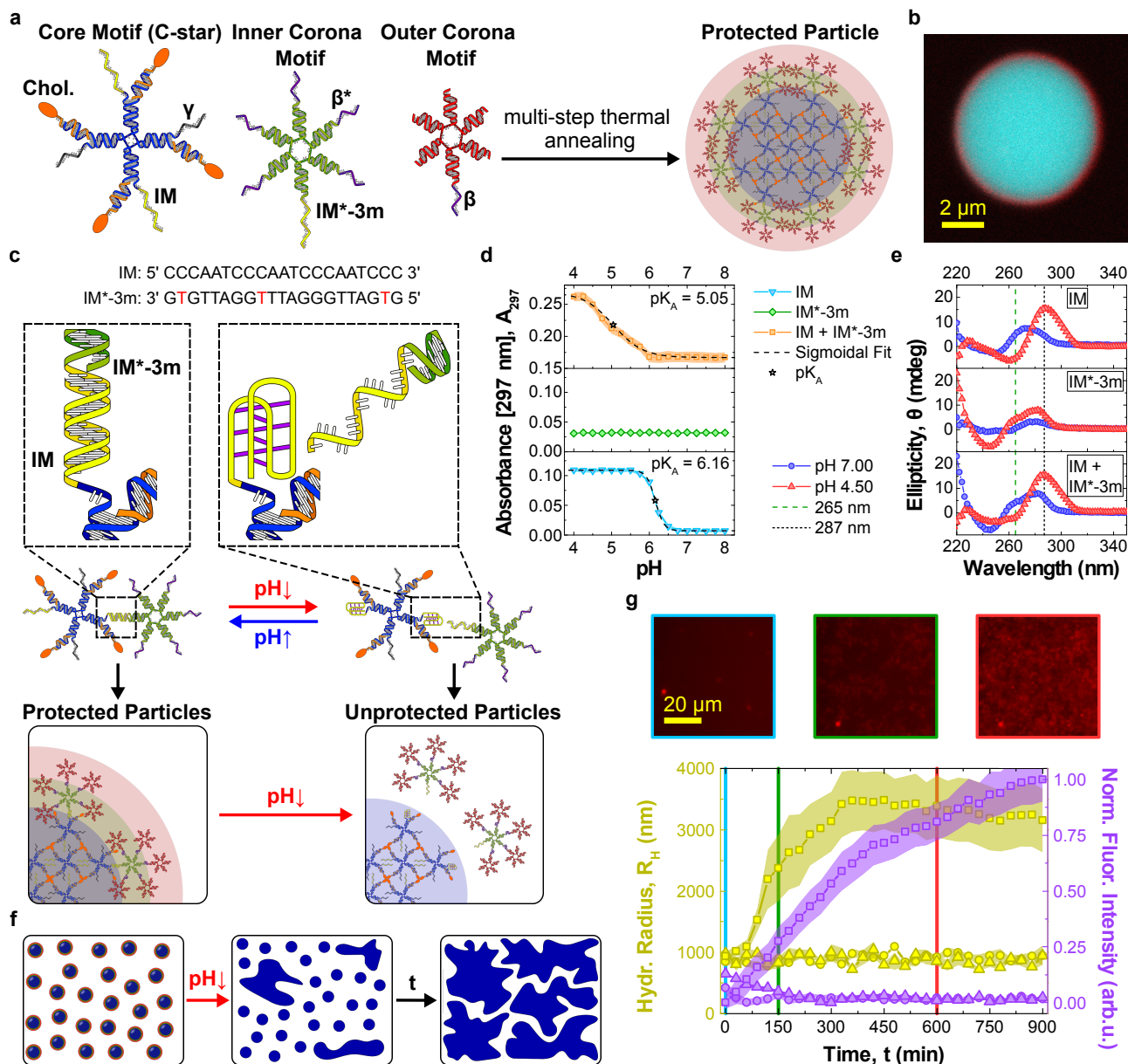


**FIG. 2. Core-shell DNA-based particles form a network in response to pH changes.** **a.** Core-shell DNA particles assemble from cholesterolised (core motifs, CMs) and non-cholesterolised DNA nanostars (inner and outer corona motifs, ICM and OCM, respectively) [54]. CMs, composed of cholesterol-functionalised (orange) and non-functionalised strands (blue), form the hydrophobic particle core. ICMs and OCMs create a stabilising corona. CMs and ICMs bind through domains  $IM$  and  $IM^* - 3m$ , while ICMs and OCMs attach through  $\beta - \beta^*$  overhangs. Domain  $\gamma$  can be used to fluorescently label CMs, by connecting to an Alexa Fluor 594-labelled duplex. When not used,  $\gamma$  is replaced by a poly-T sequence. Sequences of all strands used in this work and composition of all samples are outlined in Supplementary Tables 1 and 2, respectively. The relative thickness of core and shell region in the schematics is not in scale. **b.** Confocal micrograph of a large particle with distinguishable core-shell structure, assembled through a slow annealing protocol. Particles used in the remaining experiments had a much smaller size (200 nm – 1  $\mu\text{m}$ , see Methods). CMs are shown in cyan (fluorescein), OCMs in red (Alexa Fluor 647). **c.**  $IM$  and  $IM^* - 3m$  domains are designed to cause the detachment of ICMs from CMs at low pH.  $IM$  is C-rich, able to form a non-canonical i-motif under acidic conditions [56], resulting in destabilisation of the duplex formed by  $IM$  and  $IM^* - 3m$ . The duplex is rendered less stable by mismatches between the two sequences (red). **d.** pH-dependence of the UV absorbance at 297 nm, measured as proxy for i-motif formation [57, 58], for samples of  $IM$ ,  $IM^* - 3m$  and  $IM + IM^* - 3m$  oligonucleotides (not linked to star motifs). Increase in  $A_{297}$  marks i-motif formation achieved at pH  $\sim 6.16$  for isolated  $IM$  and  $\sim 5.05$  when also  $IM^* - 3m$  is present, with the difference ascribed to competition between duplex and i-motif formation. The transitional pH ( $pK_A$ ) values were calculated as the inflection points of sigmoidal fits. No response was observed in isolated  $IM^* - 3m$ . The data are shown as mean  $\pm$  standard error (shaded regions) of two experiments performed on two independently prepared samples, each consisting of three measurements. **e.** Circular dichroism (CD) spectra of  $IM$ ,  $IM^* - 3m$  and  $IM + IM^* - 3m$  samples. Data are averaged over three measurements. **f.** Schematic representation of pH-induced particle aggregation. pH decrease leads to i-motif formation, corona displacement, exposure of the sticky cholesterol-DNA cores, and ultimately particle aggregation. **g.** Bottom: particle aggregation after pH decrease tracked by measuring the hydrodynamic radius of growing aggregates with Differential Dynamic Microscopy (DDM, left axis) [59, 60] and the normalised epifluorescence intensity of accumulating CMs labeled with Alexa Fluor 594 (red, right axis). Triangles and squares represent responsive particles incubated at pH 7.0 (triangles) and 4.5 (squares). Circles indicate a control sample with non-responsive particles at pH 4.5, where the  $IM$  and  $IM^* - 3m$  domains have been replaced with non-responsive sequences. Data are plotted as mean  $\pm$  standard error (shaded regions) of three (circles and triangles) or six (squares) measurements conducted on two independently prepared samples. Top: epifluorescence micrographs of responsive particles after pH decrease at different time points ( $t = 0, 150$  and  $600$  min). See Supplementary Fig. 5 for additional micrographs.

1 we seek to implement here (Fig. 1b). However, multiple 57  
2 critical features are missing from the system presented 58  
3 in Ref. [54], including the ability of the particles to 59  
4 directly respond to signals generated by the target cells. 60

5  
6 Establishing this missing communication link requires 62  
7 the identification of a sufficiently general, cell-generated 63  
8 signal that can be coupled with the reconfiguration 64  
9 of the DNA nanostructures. Our model target – *E.* 65  
10 *coli* – similar to several other species, is well known to 66  
11 naturally acidify its microenvironment as a result of its 67  
12 sugar metabolism [55]. We thus identified pH as the 68  
13 ideal biogenous trigger, and proceeded to render the 69  
14 particles pH-responsive, so that the protective corona 70  
15 detaches from the sticky core at sufficiently low pH. This 71  
16 effect was obtained by engineering the DNA overhangs 72  
17 that link the CMs to the ICMS, and in particular by 73  
18 exploiting the pH-responsiveness of C-rich sequences. As 74  
19 highlighted in Fig. 2c, at neutral pH ( $\sim 7$ ), the C-rich *IM* 75  
20 domain [56] on the CM hybridises to domain *IM\** – *3m* 76  
21 on the ICM, due to them being complementary but 77  
22 for three base mismatches. At lower pH, the duplex 78  
23 formed by *IM* and *IM\** – *3m* is destabilised by the 79  
24 formation of an intra-molecular, non-canonical i-motif 80  
25 in *IM* [56, 58, 64], thus leading to separation of the CM 81  
26 from the ICM. 82

27  
28 We characterised the pH-induced i-motif-to-duplex 84  
29 transition by recording UV absorbance at 297 nm, 85  
30 known to increase following C-protonation and i-motif 86  
31 formation [57, 58]. Results, collated in Fig. 2d, show a 87  
32 transitional pH value ( $pK_A$ ) equal to 6.16 for samples 88  
33 that only contain *IM*, which is reduced to 5.05 when 89  
34 also *IM\** – *3m* is present, owing to duplex hybridisation 90  
35 counteracting i-motif formation. A similar  $pK_A$  was 91  
36 obtained with Dynamic Light Scattering measurements 92  
37 assessing the pH-dependent complexation of CMs and 93  
38 ICMS, as shown in Supplementary Fig. 4. i-motif forma- 94  
39 tion was further confirmed by Circular dichroism (CD), 95  
40 as summarised in Fig. 2e. At pH 4.50, samples contain- 96  
41 ing *IM*, both with and without *IM\** – *3m*, produced 97  
42 CD spectra with a maximum at 287 nm and minimum 98  
43 at 265 nm, both characteristic of the i-motif [57]. In 99  
44 traces recorded at pH 7.00, both extremes were shifted 100  
45 to lower wavelengths, as expected for dsDNA. 101

46  
47 pH-induced corona displacement causes the exposure 102  
48 of the particles' sticky cores, leading to their cholesterol- 103  
49 mediated aggregation and the formation of an extended 104  
50 amphiphilic DNA network, as shown in Fig. 2f. To 105  
51 assess network formation we used Differential Dynamic 106  
52 Microscopy (DDM) [59, 60], which allowed the monitor- 107  
53 ing of the time-evolution of the hydrodynamic radius 108  
54 of the particles,  $R_H$ , after lowering the pH to 4.5. The 109  
55 data, collated in Fig. 2g (left axis, squares), show the 110  
56 expected increase in  $R_H$  from the initial value of  $\sim 1 \mu\text{m}$ , 111

resulting from particle aggregation. Network formation 112  
is visible in epifluorescence micrographs collected using 113  
particles labelled with Alexa 594 (Fig. 2g, top). The 114  
mean (normalised) fluorescence intensity from the micro- 115  
graphs can further be used to track particle aggregation, 116  
exploiting progressive sedimentation of the aggregates 117  
that leads to an increase in the fluorescent signal close 118  
to the bottom of the imaging well. The fluorescence 119  
traces shown in Fig. 2g (right axis, squares), expectedly, 120  
follow a trend similar to the hydrodynamic radius. 121  
To confirm the specificity of the observed aggregation 122  
response, we conducted two control experiments, one 123  
in which pH responsive particles were kept at pH 7 124  
(triangles) and another where non-responsive particles, 125  
obtained by replacing the C-rich motif with a sequence 126  
unable to form an i-motif, were exposed to pH 4.5 127  
(circles). In both controls, no aggregation was noted 128  
from the  $R_H$  or fluorescence intensity data (Fig. 2g), 129  
confirming that the observed network formation indeed 130  
emerges from the designed pH-responsive pathway. 131  
The absence of non-triggered aggregation, also con- 132  
firmed for medium compositions different from PBM9 133  
(Supplementary Fig. 6), demonstrates the stability 134  
of the particles in bare media over experimentally 135  
relevant timescales. An extended set of bright field and 136  
epifluorescence micrographs, showing the behaviour of 137  
responsive/nonresponsive particles at neutral and acidic 138  
pH, is included in Supplementary Fig. 5. 139

### Bacteria immobilisation triggered by glucose metabolism in *E. coli*

Acidification of the extracellular milieu is a very com- 140  
mon phenomenon, as a vast number of microorganisms 141  
produce acids as a consequence of fermentative processes. 142  
Particularly notable among them are bacteria belonging 143  
to the Bacillota and Pseudomonadota phyla that include 144  
human pathogens such as *Pseudomonas aeruginosa*, 145  
*Enterococcus faecalis*, *Salmonella enterica*, *Streptococcus* 146  
*pneumoniae*, *Yersinia pestis* and *Escherichia coli* [55]. 147  
Due to its high tractability in lab settings, we set 148  
out to demonstrate our synthetic netosis-like pathway 149  
in the presence of *E. coli*, which excretes acetate as 150  
a result of glucose metabolism thereby acidifying its 151  
growth medium, as sketched in Fig. 3a. Having designed 152  
responsive DNA-based particles capable of forming a 153  
sticky network upon exposure to acidic conditions, we 154  
proceed to determine whether *i)* the particles can be 155  
“activated” by glucose metabolism in *E. coli* and *ii)* the 156  
formed network can trap the cells, as required for the 157  
synthetic netosis-like response outlined in Fig. 1 (right). 158

As demonstrated in Fig. 3b (left), the magnitude of 159  
the pH decrease in *E. coli* cultures can be modulated 160

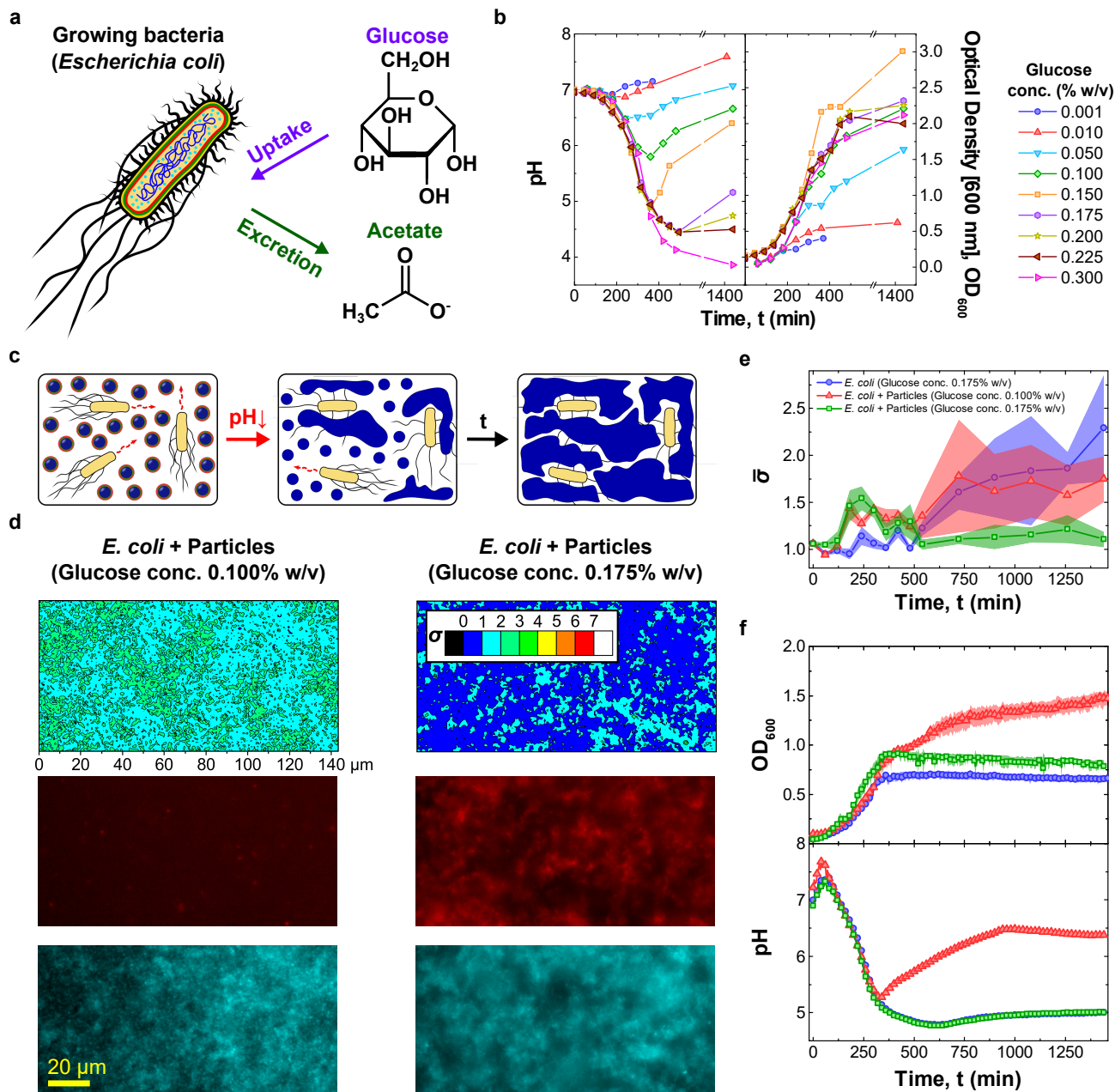


**FIG. 3. pH-responsive DNA particles trap *E. coli* when triggered by bacterial metabolism** **a.** Glucose metabolism in *E. coli* leads to acetate release and pH decrease [55]. **b.** (left) Bacteria-induced pH changes depend on glucose concentration in the medium,  $\rho_G$ . For intermediate values ( $0.050\% \text{ w/v} \leq \rho_G \leq 0.200\% \text{ w/v}$ ) the pH decreases and reaches a minimum before recovering. For  $\rho_G \geq 0.225\% \text{ w/v}$  recovery is not observed. Glucose concentration influences bacterial growth, quantified through turbidity ( $\text{OD}$ ) measurements at 600 nm (right). Culture yield increases with  $\rho_G$ , is maximised at intermediate values, and decreases at higher glucose concentration, possibly due to excessive medium acidification. Data for  $\rho_G = 0.175, 0.200$  and  $0.225\% \text{ w/v}$  are shown as average of three independent repeats, the remaining points are from a single repeat. **c.** Diagram illustrating *E. coli* trapping by the synthetic DNA net. Bacterial metabolism reduces the pH, causing particle activation and the formation of a sticky network (Fig. 2) that embeds the cells. **d.** (top) *E. coli* immobilisation induced by DNA net formation as quantified through the motility parameter  $\sigma$ , extracted from bright field microscopy videos (see Methods). The two colourmaps are relative to samples containing *E. coli*, responsive particles and different  $\rho_G$  values, one insufficient ( $0.100\% \text{ w/v}$ , left) and the second sufficient ( $0.175\% \text{ w/v}$ , right) to reach the pH threshold for particle activation ( $5.05$ , see Fig. 2d). Bottom: epifluorescence micrographs corresponding to the  $\sigma$ -maps. Core motifs are labelled with Alexa Fluor 594 (red), while *E. coli* express EGFP (cyan). Smaller  $\sigma$ -values and co-localisation of DNA and bacteria observed in the sample with higher glucose concentration confirm the ability of cholesterol-DNA networks to bind and immobilise *E. coli*.  $\sigma$ -maps and images were collected at  $t = 1440$  min after sample preparation. **e.** Time evolution of the frame averaged motility parameter  $\bar{\sigma}$  recorded for the samples in panel d and a control sample with *E. coli* and  $\rho_G = 0.175\% \text{ w/v}$ , but lacking DNA particles. The decrease in  $\bar{\sigma}$  noted in the sample with responsive particles and higher glucose concentration confirms reduced *E. coli* motility following trapping. Data are shown as mean  $\pm$  standard error of seven measurements conducted on three independent repeats. Associated  $\sigma$ -maps and epifluorescence micrographs are shown in Supplementary Fig. 11. **f.** Time-traces of  $\text{OD}_{600}$  (top) and medium pH (bottom) for the three samples in panel e. The pH was measured using the ratiometric pH probe FITC-dextran, added in solution (see Supplementary Figs 9 and 10, and Methods). For both  $\text{OD}$  and pH, data are shown as averages of three independent repeats. For the  $\text{OD}$  curves, standard errors are shown as shaded regions.

1 by changing the initial concentration ( $\rho_G$ ) of glucose 57  
2 in the medium. For all but the lowest tested glucose 58  
3 concentrations (0.001% and 0.01% w/v) a notable 59  
4 decrease in pH was observed, followed by a recovery 60  
5 for  $\rho_G \leq 0.200\%$  w/v due to re-uptake of acetate at 61  
6 later growth stages [55]. The magnitude of the pH drop 62  
7 correlates with glucose concentration, with values lower 63  
8 than 5, required for particle activation, reached when 64  
9  $\rho_G \gtrsim 0.150\%$  w/v. Figure 3b (right) explores the link be- 65  
10 tween glucose concentration and cell growth, quantified 66  
11 through optical density (600 nm). The highest yield was 67  
12 observed for  $\rho_G = 0.150\%$  w/v, with lower yields noted 68  
13 for both higher and lower  $\rho_G$  values. The substantially 69  
14 lower yield seen at high  $\rho_G$  (0.300% w/v) correlates 70  
15 with the lack of recovery in pH observed in Fig. 3b 71  
16 (left), hinting that excessive acidification may impact 72  
17 *E. coli* metabolism and prevent acetate re-uptake. In 73  
18 Supplementary Figs 7 and 8 we present OD and pH 74  
19 data collected for *E. coli* cultured in well plates, relevant 75  
20 for the synthetic netosis experiments discussed below 76  
21 (see Methods). Trends similar to those reported in 77  
22 Fig. 3b for flask cultures were noted, both in terms of 78  
23 growth curves and pH traces. A systematic difference 79  
24 was observed in the lowest pH reached for  $\rho_G = 0.300\%$  80  
25 w/v, which was higher in well plates compared to 81  
26 flask experiments ( $\sim 4.75$  and  $\sim 4$ , respectively). This 82  
27 deviation is likely due to the different method used to 83  
28 record pH, which relied on a physical pH probe in flasks 84  
29 and on a ratiometric fluorescent probe, FITC-dextran, 85  
30 in well plates. The response of the fluorescent probe 86  
31 was indeed found to saturate at pH  $\sim 5$  (Supplementary 87  
32 Fig. 9). We note that, to preserve the buffer conditions 88  
33 optimised for particle assembly and stability, bacteria 89  
34 were cultured in a newly developed medium dubbed 90  
35 PBM9. Medium composition, outlined in the Methods 91  
36 section, was selected to match ionic and buffering 92  
37 properties of PBS buffer and contain compounds needed 93  
38 to support bacterial growth, as in the M9 medium. 94

39  
40 Having characterised the ability of *E. coli* to acidify 96  
41 their medium, we proceeded to test DNA-particle acti- 97  
42 vation and consequent bacteria trapping. As sketched 98  
43 in Fig. 3c, the pH-responsive particles were deployed 99  
44 in *E. coli* samples with  $\rho_G = 0.175\%$  w/v, sufficient 100  
45 to achieve the pH-level required for particle activation, 101  
46 and  $\rho_G = 0.100\%$ , insufficient to reach the threshold 102  
47 (compare Fig. 2d (top) and Fig. 3b (left)). We note that 103  
48 the two  $\rho_G$  values result in comparable growth rates 104  
49 (Fig. 3b, right). 105

50  
51 Epifluorescence images of both particles (red) and 107  
52 bacteria (cyan), collected after incubating the samples 108  
53 for  $t = 1440$  minutes, are shown Fig. 3d (bottom). 109  
54 The snapshots readily demonstrate formation of the 110  
55 synthetic DNA net in the sample with higher glucose 111  
56 concentration, while no visible particle aggregation 112

was seen for  $\rho_G = 0.100\%$ . We can thus confirm that  
metabolism-induced acidification is capable of triggering  
particle aggregation, establishing the sought commu-  
nication link between the cells and the synthetic DNA  
constructs. To assess whether the DNA net displays the  
desired ability to trap motile *E. coli*, a parameter  $\sigma$  was  
extracted from high-framerate bright-field microscopy  
videos of the samples, defined as the time-averaged  
standard deviation of the pixel-intensity computed  
over seven consecutive frames (see Methods). We  
have previously demonstrated that  $\sigma$  represents a good  
proxy for bacterial motility, taking larger values in  
samples of motile *E. coli* and lower values if the cells  
are immobilised [54]. A clear difference in  $\sigma$  between  
the sample with lower and higher  $\rho_G$  is notable from the  
colormaps in Fig. 3d (top), relative to the end-point of  
our experiments ( $t = 1440$  minutes). The substantial  
reduction in bacterial motility observed for  $\rho_G = 0.175\%$   
confirms that the DNA-particles were able to trap *E. coli*,  
once activated by the bacteria themselves, hence  
confirming two-way particle-cell communication.

The relative homogeneity of  $\sigma$  across the fields of view  
allows us to track the time evolution of bacteria motility  
by monitoring the frame-averaged  $\bar{\sigma}$ , as summarised  
in Fig. 3e for the two samples discussed in Fig. 3d.  
A control *E. coli* sample with  $\rho_G = 0.175\%$  w/v,  
but lacking DNA particles, is also included. After  
initial fluctuations,  $\bar{\sigma}$  increases in the sample with  
 $\rho_G = 0.100\%$  w/v and in the control sample, as a result  
of the increase in number of cells (compare Fig. 3b) and  
the lack of physical constraints limiting their motility.  
In contrast, in the sample containing particles, under  
conditions supporting their activation ( $\rho_G = 0.175\%$   
w/v),  $\bar{\sigma}$  decreases at  $t = 510$  min before plateauing at  
 $t = 720$  min, as a consequence of DNA net formation  
and bacteria trapping. The onset of net formation  
correlates with the time-evolution of the pH reported  
in Fig. 3f (bottom), showing that the pH threshold  
required for particle activation (5.05) was reached  
prior to the time at which  $\bar{\sigma}$  decreased. pH data were  
recorded with the fluorimetric probe FITC-dextran.  
See Supplementary Figs 9 and 10 for the calibration  
curve and raw fluorescence data, respectively. Both the  
pH trends and the OD growth curves shown in Fig. 3f  
(bottom and top, respectively) closely match data  
collected in samples lacking particles (Supplementary  
Fig. 8), indicating that particles have negligible effect  
on bacterial growth and metabolism under the tested  
conditions. Epifluorescence images and  $\sigma$  color-maps for  
the three samples discussed in Fig. 3e-f are shown in  
Supplementary Fig. 11 for selected time-points, enabling  
visual assessment of the difference in sample evolution  
resulting from net formation and bacteria trapping.

The modularity of our DNA nanodevices allowed us

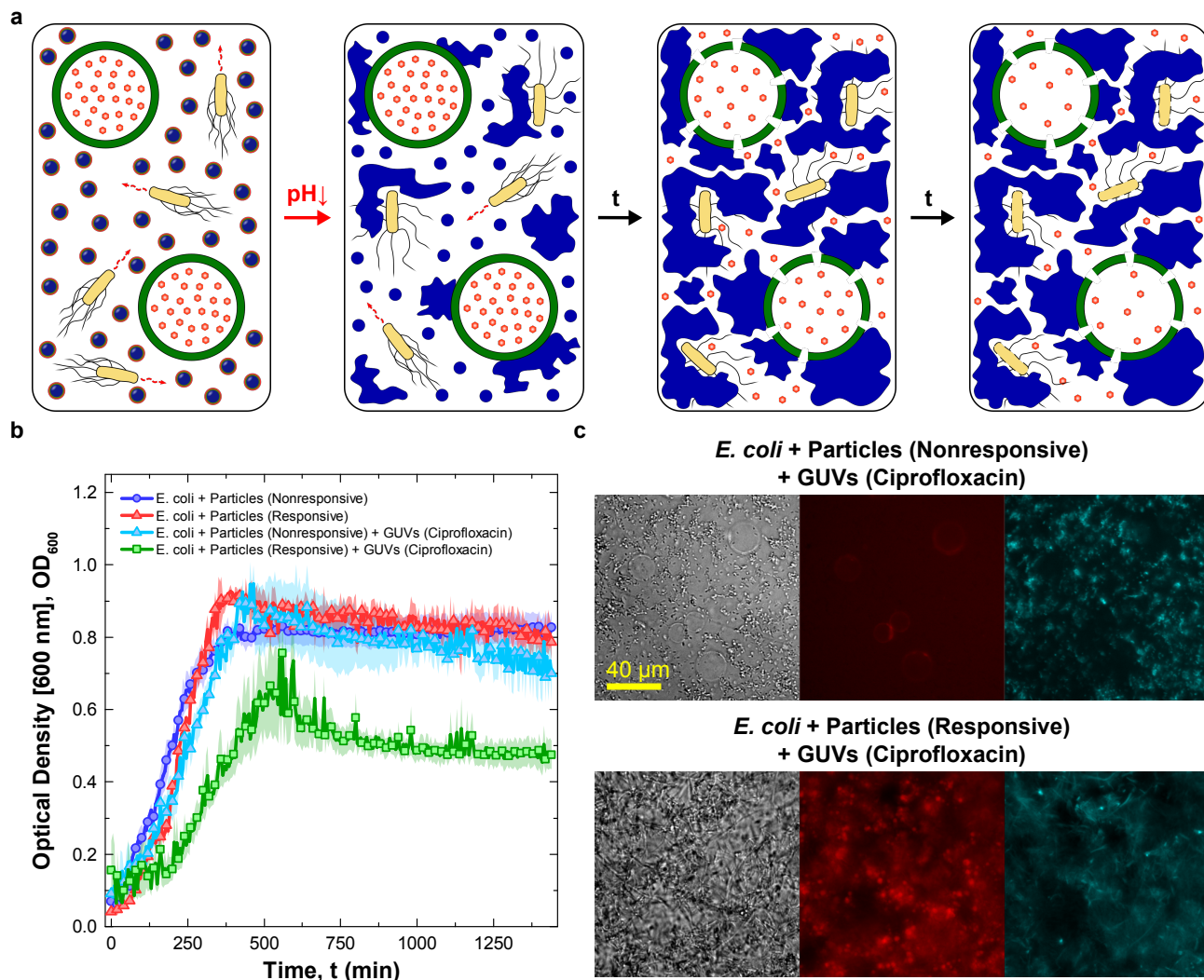


**FIG. 4. Synthetic cell signalling network produces netosis-like response** **a.** Diagram illustrating the mechanism of action of the synthetic signalling network producing a netosis-like response. Medium acidification caused by *E. coli* glucose metabolism activates the DNA-particles. The particles form a sticky DNA-cholesterol network that, simultaneously, traps the bacteria and permeabilises Giant Unilamellar Vesicles (GUVs) loaded with antibiotic ciprofloxacin. The released antibiotic hinders bacterial growth. **b.** Antimicrobial response as determined *via* turbidity measurements (OD at 600 nm). Data are shown for four samples as the mean of three independent repeats  $\pm$  standard errors (shaded regions). One sample includes *E. coli*, antibiotic-loaded GUVs, responsive particles, and sufficient glucose to achieve their activation ( $\rho_G = 0.175\%$  w/v), and is thus capable of supporting the cascade of reactions producing the sought netosis-like response (green squares). The other three samples are controls missing one or more key components. Two control samples lack antibiotic-loaded GUVs, and feature either non-responsive (blue circles) or responsive (red triangles) DNA particles. The third control sample contains antibiotic-loaded GUVs but uses non-responsive particles. While all control samples show similar OD curves, growth is delayed and suppressed in the system capable of sustaining the designed cascade of reactions. **c.** Bright field and epifluorescence micrographs of samples containing *E. coli*, nonresponsive (top) or responsive (bottom) particles and ciprofloxacin-loaded GUVs, recorded at  $t = 1440$  min after sample preparation. Aggregation of DNA and the lack of GUVs in the sample with responsive particles indicates the successful rupture of vesicles following DNA-net formation. The released antibiotic hinders *E. coli* division, causing cell elongation. Particles (core motifs) are shown in red (Alexa Fluor 594), *E. coli* in cyan (EGFP). See Supplementary Fig. 16 for additional bright field and epifluorescence micrographs recorded at  $t = 0$  and 1440 min.

1 to introduce additional functionality in the bacteria- 7  
 2 trapping DNA particles. This is exemplified in Supple- 8  
 3 mentary Figs 12 and 14, where we tested design varia- 9  
 4 tions of the particles that enable *in situ* fluorescent re- 10  
 5 porting of the bacteria-induced pH change, and conse- 11  
 6 quent particle activation. In Supplementary Fig. 12, pH 12

sensing was achieved by linking the ratiometric pH probe  
 FITC-dextran to the core motifs. Observed trends were  
 similar to the ones obtained with probes freely diffusing  
 in bulk (Fig. 3f and Supplementary Fig. 10), but with  
 the advantage that the labelled particles can probe pH  
 in the local DNA-net microenvironment, in the vicinity of

1 trapped bacteria. See also the calibration curve in Sup- 54  
2 plementary Fig. 13. In Supplementary Fig. 14, instead, 55  
3 we detected the pH-induced detachment of the corona 56  
4 motifs from the core motifs by placing a fluorophore and 57  
5 quencher on the *IM* and *IM\** - *3m* domains, respec- 58  
6 tively. The biosensing capabilities of the material could 59  
7 be potentially further expanded by including agents that 60  
8 monitor alternative metabolic processes, *e.g.* Fe(III) res- 61  
9 piration metabolism, as reported by Chen *et al.* [65]. 62

## 10 **Bacterial growth inhibition induced by the synthetic** 65 11 **netosis-like pathway** 66

12 With the pH-responsive DNA particles we have 68  
13 successfully replicated two of the key responses of 69  
14 netosis, namely the detection of target cells and their 70  
15 immobilisation in a sticky DNA-cholesterol network. 71  
16 One last property is missing to fully mimic the biological 72  
17 response, and that is the antimicrobial action of the 73  
18 neutrophil extracellular traps causing cell death in 74  
19 the trapped pathogens. As observed above, however, 75  
20 the synthetic cholesterol-DNA net does not suppress 76  
21 bacterial growth under the tested conditions. Hence, 77  
22 to endow the system with antimicrobial properties, we 78  
23 introduced a second synthetic agent: a GUV loaded 79  
24 with the antibiotic ciprofloxacin, as sketched in Fig. 1b. 80  
25 The antibiotic was chosen due to its low minimum 81  
26 inhibitory concentration (MIC, Supplementary Fig. 15), 82  
27 and encapsulated within the GUVs at 200× this value 83  
28 ( $3.2 \mu\text{g mL}^{-1}$ ). The designed netosis-like response of the 84  
29 resulting three-agent artificial consortium is graphically  
30 outlined in Fig. 4a: after *E. coli*-induced medium  
31 acidification, the unprotected particles are expected to  
32 bind to the GUV and either disrupt or permeabilise  
33 them, causing the release of the drug that would, in turn, 86  
34 hinder the growth of trapped bacteria. The ability of 87  
35 unprotected cholesterol-DNA particles to render GUVs 88  
36 permeable has been tested in our previous contribution, 89  
37 using a fluorescent probe [54]. 90

38  
39 To evaluate the antimicrobial action of the drug-loaded 92  
40 GUVs, and thus validate the netosis-like response of our 93  
41 synthetic consortium, we conducted an assay in which 94  
42 GUVs and pH-responsive particles were deployed in an 95  
43 *E. coli* sample along with 0.175% w/v glucose, sufficient 96  
44 to induce particle activation thorough medium acidifica- 97  
45 tion (Fig. 3). The resulting OD growth curve is shown 98  
46 in Fig. 4b (green squares), and compared with data from 99  
47 three distinct control experiments where we selectively 100  
48 eliminated components and functionalities required for 101  
49 the antimicrobial response. These include samples in 102  
50 which GUVs were not present and particles were either 103  
51 non-responsive (blue circles) or pH-responsive (red tri- 104  
52 angles), or where the GUVs were present along with 105  
53 non-responsive particles (cyan triangles). All control ex- 106

periments produced similar growth curves, providing a  
baseline and confirming that neither the particles (re-  
sponsive or non responsive), nor undisturbed antibiotic-  
loaded GUVs, influence growth. The sample sustaining  
the complete netosis-like pathway, instead, produced a  
visibly different response. While growth is similar to the  
controls in the initial two hours, once acidification and  
consequent particle activation occur, growth slows down  
leading to a maximum OD lower compared to the con-  
trols, followed by a noticeable decrease in OD at later  
times. A visual insight in the response of the systems  
can be gained from the bright field and epifluorescence  
images in Fig. 4c, collected at the end of the experiments  
(1440 minutes from sample preparation). Here, the con-  
trol sample featuring GUVs and non-responsive particles  
is compared with the complete netosis-like system. In  
the control, no DNA net was formed (red epifluorescence  
channel) and the GUVs clearly retained their structural  
integrity (bright field) despite weak interactions with the  
non-activated particles (red channel). Bacteria also re-  
tained their physiological rod-like shape (bright field and  
cyan epifluorescence channel). Instead, in the sample ca-  
pable of sustaining the full cascade of reactions leading  
to netosis, GUVs were no longer visible, having been dis-  
rupted by the formed DNA net. The consequent release  
of antibiotic had a clear effect the ability of *E. coli* to di-  
vide, as the cells acquired a visible filamentous morphol-  
ogy. The microscopy data, along with additional images  
provided in Supplementary Fig. 16, confirm the ability  
of our synthetic consortium to sustain the designed re-  
sponses leading to the sought netosis-like mechanism.

## DISCUSSION

In this work we reported the bottom-up construction  
of a synthetic signalling network capable of imitating  
a complex immune response, namely that of netosis.  
Through this process, neutrophils detect, trap, and kill  
pathogens by secreting a DNA-based extracellular trap.  
Our artificial netosis pathway relies on the action of  
DNA-based synthetic particles, which upon detecting  
bacteria-induced medium acidification, form a sticky  
network reminiscent of the biological trap, capturing the  
cells. Simultaneously, the particles cause antibiotic to be  
released from liposomes, hindering growth and division  
in the trapped cells.

The netosis-like behaviour emerges from the coor-  
dinated activation of multiple biomimetic functions,  
including biosensing, morphological adaptation and  
communication, exemplifying how advanced life-like  
responses can be implemented with a relatively small  
number of molecular components, exploiting the  
modularity and programmability of nucleic-acid nan-  
otechnology. Inspired by our solution, similar synthetic



1 pathways could be implemented to program responses 53  
2 in the bacterial communities different from their death, 54  
3 for instance by loading the liposomes with inducers trig- 55  
4 gering protein synthesis [50], exploiting the cell-trapping 56  
5 functionality to engineer multi-species microbial con- 57  
6 sortia [66], or scaffolding synthetic biofilms, valuable in 58  
7 biomaterial synthesis [67] and bioremediation [68, 69]. 59  
8 The resulting “living biomaterials” [70], may also feature 60  
9 rheological properties which are dependent on the 61  
10 activity of the trapped cells, deserving future investiga- 62  
11 tion [71]. Matrix rheology could, in turn, influence cell 63  
12 growth [72], enabling the design of adaptable materials  
13 reliant on biomechanical feedback loops.

14  
15 Besides pushing the boundaries of bottom-up syn-  
16 thetic biology, our implementation could underpin 65  
17 disruptive antimicrobial solutions that, like our natural 66  
18 immunity, benefit from the combination of physical (cell 67  
19 immobilisation) and chemical (antibiotics) modes of 68  
20 action. To this end, activation of the synthetic net could 69  
21 be rendered conditional to pathogen-associated stimuli 70  
22 other than pH, such as the presence of cell-surface 71  
23 antigens [73] or soluble biomarkers [74], exploiting 72  
24 base-pairing, aptamer technology or functionalisation 73  
25 with chemical or biological ligands. Solutions could 74  
26 also be devised to integrate the cargo-loaded liposomes 75  
27 and DNA-particles in a single agent, exploiting well- 76  
28 established strategies to link DNA devices to lipid 77  
29 membranes [75, 76]. The resulting “synthetic immune 78  
30 cell” could be valuable beyond antimicrobials, and 79  
31 be adapted to tackle, *e.g.*, inflammation or cancer by 80  
32 adjusting the therapeutic payload and trigger stimulus, 81  
33 building towards the ambitious goal of creating effective 82  
34 and robust synthetic cellular therapies [42]. 83  
35

## 36 METHODS

### 37 Design and handling of DNA strands

38 DNA nanostructures were designed in NUPACK [77]. 91  
39 A constraint forbidding more than three consecutive C 92  
40 or G bases was imposed to inhibit formation of un- 93  
41 wanted secondary structures. The i-motif forming do- 94  
42 main and its complement were excluded from this con- 95  
43 straint. All sequences are provided in Supplementary 96  
44 Table 1. Core Strand 1, carrying the internal Rho- 97  
45 damine 6G modification was purchased from Eurogen- 98  
46 tec. All remaining strands were bought from Inte- 99  
47 grated DNA Technologies (IDT). The functionalised and 100  
48 non-functionalised oligonucleotides were purified by the 101  
49 supplier using high-performance liquid chromatography 102  
50 (HPLC) and standard desalting, respectively. Once 103  
51 delivered, the dehydrated DNA was reconstituted in 104  
52 phosphate-buffered saline (PBS, 137 mM NaCl, 2.7 mM 105

KCl, 8 mM Na<sub>2</sub>HPO<sub>4</sub>, 2 mM KH<sub>2</sub>PO<sub>4</sub>, pH 7.4, Invitro-  
gen, Thermo Fisher Scientific). To remove any large par-  
ticulate contaminants the solutions of non-functionalised  
oligonucleotides were syringe-filtered with polyethersul-  
fone filters (0.22 μm pore size, Millex). The concentra-  
tion of reconstituted DNA samples was determined by  
measuring the absorbance at 260 nm on a Thermo Scien-  
tific Nanodrop 2000 UV-Vis spectrophotometer. The ex-  
tinction coefficients were provided by the supplier (IDT)  
or calculated using the OligoAnalyzer online tool from  
IDT. All stock solutions were stored at -20°C.

### 64 Preparation of non-functionalised DNA structures

Samples used to probe the folding efficiency, correct  
binding, thermal stability and pH-responsiveness of  
individual nanostructures were prepared from non-  
functionalised strands to prevent aggregation mediated  
by hydrophobic moieties. To achieve this, all the  
cholesterol-functionalised oligonucleotides were replaced  
with non-modified strands of identical sequence.  
Concentrated solutions of DNA strands in PBS were  
prepared by stoichiometrically mixing all the required  
oligonucleotides in 200 μL DNase free Eppendorf tubes.  
Note that, at this stage, the concentration of DNA  
strands was set to be 2× or 2.15× higher as compared  
to the final values given in Supplementary Table 2, to  
allow introduction of the M9 component of the PBM9  
medium (see relevant Methods section below) and pH  
adjustment. Prepared mixtures were placed in a Techne  
TC-512 thermal cycler, heated up to 95°C, held at this  
temperature for 5 min, and then cooled down to 20°C  
at the rate of -0.05°C min<sup>-1</sup> to enable nanostructure  
assembly.  
55 Samples for agarose gel electrophoresis (AGE) and UV  
56 melting curves of non-cholesterolised DNA structures  
57 (60 μL and 600 μL, 2× DNA concentration) were  
58 transferred into 1.5 mL DNase free Eppendorf tubes  
59 and mixed in equal volumes with a solution containing  
60 PBS buffer, 37.4 mM NH<sub>4</sub>Cl, 0.2 mM CaCl<sub>2</sub>, 4 mM  
61 MgSO<sub>4</sub>, 0.4% w/v casamino acids (CAAs) and 0.35%  
62 w/v glucose (pH 6.54), termed PB(2×)M9, to obtain 1×  
63 DNA concentration in PBM9 medium (pH 7.00).  
64 For the preparation of samples for dynamic light scat-  
65 tering (DLS), UV-vis absorbance, and circular dichroism  
66 (CD) of non-functionalised DNA nanostructures, 700  
67 μL of 2.15× concentrated solutions of assembled DNA  
68 nanostructures were placed in 50 ml centrifuge tubes  
69 (Greiner Bio-One) and supplemented with 700 μL of  
70 PB(2×)M9. Afterwards, their pH was tuned with  
71 hydrochloric acid (HCl, 1 M or 6 M, Sigma-Aldrich) or  
72 potassium hydroxide (KOH, 1 M or 5 M, Sigma-Aldrich)  
73 solutions using a bench-top pH meter (pH 210, Hanna  
74 Instruments) equipped with a double junction pH  
75 electrode (9110DJWP, Orion). Finally, their volume was

1 adjusted to 1500  $\mu\text{L}$  by adding milli-Q water. 50  
2 All the prepared samples were stored at 4°C and used 51  
3 within 24 h. 52  
4

## 5 Preparation of pH-responsive particles

6 DNA strands were mixed in stoichiometric ratio in 61  
7 PBS to the final concentration of core strands equal 62  
8 to 1  $\mu\text{M}$  (concentrations of all the oligonucleotides are 63  
9 listed in Supplementary Table 2), in 500  $\mu\text{L}$  DNase free 64  
10 Eppendorf tubes. The overall sample volume was set to 65  
11 60  $\mu\text{L}$  or 200  $\mu\text{L}$ , depending of the annealing protocol 66  
12 used. 67

13 Small volumes (60  $\mu\text{L}$ ) of the samples used to prepare 68  
14 large particles (Fig. 1b), were loaded into borosilicate 69  
15 glass capillaries (inner section of 4 mm  $\times$  0.4 mm, CM 70  
16 Scientific). The capillaries were previously cleaned by 71  
17 sonicating for 15 min once in a 2% Hellmanex III water 72  
18 solution (Hellma Analytics) and then twice in milli-Q  
19 water. Both ends of the capillaries were capped with  
20 mineral oil, and sealed shut and attached to microscope 73  
21 slides (Menzel Gläser, 24 mm  $\times$  60 mm, No. 1) with 74  
22 fast-drying epoxy glue (Araldite). Sealed capillaries were  
23 then placed in a custom-made Peltier-controlled water 75  
24 bath and heated up to 90°C. After incubating for 30 76  
25 min, the samples were cooled down to 63°C at the rate 77  
26 of  $-0.01^\circ\text{C min}^{-1}$  and finally brought down to 20°C at 78  
27  $-0.1^\circ\text{C min}^{-1}$ . 79

28 pH-responsive particles of controlled size were prepared 80  
29 in a custom-made Peltier-controlled aluminium chamber 81  
30 allowing rapid temperature changes. 200  $\mu\text{L}$  volumes of 82  
31 the DNA strand mixtures were pipetted into ExtraSil 83  
32 (ES) quartz cuvettes (350  $\mu\text{L}$ , 1 mm path length, 10 84  
33 mm inside width, Aireka Cells) using gel-loading pipette 85  
34 tips (1-200  $\mu\text{L}$ , 0.5 mm thick round end, RNase/DNase 86  
35 free, Corning). Loaded cuvettes were placed in the 87  
36 aluminium chamber, heated up to 90°C and incubated 88  
37 for 15 min. The samples were then cooled down to  
38 65°C at  $-1^\circ\text{C s}^{-1}$  and held at this temperature for a  
39 growth time  $t_g = 15, 600$  or  $900$  s depending on the 89  
40 desired particle size. Subsequently, the temperature was 90  
41 decreased to 35°C at  $-1^\circ\text{C s}^{-1}$ , held at this value for  
42 15 min to facilitate corona formation and then further 91  
43 decreased to 20°C at the same rate. The particles can be 92  
44 melted and re-annealed multiple times, and we expect 93  
45 that one should be able to re-assemble the particles after 94  
46 pH-induced network formation, as long as the pH is 95  
47 brought back to the initial value and the DNA density 96  
48 is not substantially altered. 97  
49

## Agarose gel electrophoresis of non-functionalised DNA motifs

52 AGE was used to assess the correct folding and binding  
53 of non-functionalised DNA motifs as shown in Supple-  
54 mentary Fig. 1.

55 Samples of annealed DNA nanostructures, prepared as  
56 described above, were first mixed with 4  $\mu\text{L}$  of loading  
57 dye (Thermo Fisher Scientific) and then diluted in Tris-  
58 borate-EDTA (TBE) buffer (pH 8.3, 89 mM Tris-borate,  
59 2 mM EDTA, Sigma-Aldrich) to the final DNA concen-  
60 tration of 75 ng  $\text{mL}^{-1}$ .

Agarose gels were prepared at 1.5% w/v agarose (Sigma-  
Aldrich) in TBE buffer supplemented with SYBR safe  
DNA gel stain (Invitrogen, Thermo Fisher Scientific).  
Wells were filled with small volumes (10  $\mu\text{L}$ ) of diluted  
samples, equivalent to 750 ng of DNA. The two outermost  
wells carried a 100 bp DNA reference ladder (Thermo  
Fisher Scientific). Gels were run for 120 min at 75 V (3  
V  $\text{cm}^{-1}$ ), and then imaged using a GelDoc-It imaging  
system.

The collected images were analysed through a tailor-  
made Matlab script to obtain the integrated line intensity  
profiles.

## Dynamic light scattering of non-cholesterolised nanostar structures

DLS was used to both validate the successful assembly  
of non-cholesterolised DNA nanostructures and examine  
their stability at acidic pH (see Supplementary Fig. 2).  
First, an ultra low volume quartz cuvette (ZEN2112,  
Malvern) was loaded with 120  $\mu\text{L}$  of annealed sample  
in PBM9 medium with preadjusted pH that was set to  
either 7.0 or 4.5. Afterwards, three measurements, each  
consisting of fifteen data runs, were taken at room tem-  
perature with a Malvern Zetasizer Nano ZSP analyzer  
(scattering angle fixed at 173°, 633 nm He-Ne laser).  
For each of the visible bands, the hydrodynamic diam-  
eter  $D_H$  was determined by fitting the experimental data  
to a lognormal distribution function and then calculating  
the maximum of the fit, using a custom Matlab script.

## UV melting curves of non-functionalised DNA structures

UV-Vis spectrophotometry was used to assess the  
separation of melting temperatures  $T_M$  of core-forming  
motifs and corona-binding domains (Supplementary  
Fig. 3), required by the multi-step thermal annealing  
process used to form core-shell particles.

Large volumes (1200  $\mu\text{L}$ ) of samples containing non-  
functionalised DNA structures, prepared according  
to the protocol reported above, but excluding the

annealing step, were loaded into quartz cuvettes. To prevent evaporation, 300  $\mu\text{L}$  of mineral oil were carefully pipetted on top of each sample before sealing the cuvettes with Parafilm-wrapped polytetrafluoroethylene (PTFE) stoppers. Samples were first cooled down from 95°C to 20°C and then heated back up to 95°C at the rate of  $\pm 0.02^\circ\text{C min}^{-1}$  while their absorbance at 260 nm was measured on a temperature-controlled Varian Cary 50 UV-Vis spectrophotometer.  $T_M$  was determined with a custom Matlab script for both the cooling and heating ramps by fitting the upper and lower plateaus with straight lines and then computing the intersection between their median and the experimental data *via* interpolation [78].

### Confocal microscopy of large core-shell particles

Confocal microscopy images of large particles (Fig. 2b) were obtained with a Leica TCS SP5 laser scanning confocal microscope equipped with a HC PL APO CORR CS 40 $\times$ /0.85 dry objective (Leica). Aggregates, prepared according to the procedure described above, were extracted from the capillary by cutting open its ends with a diamond scribe, placing it in 1.5 mL DNase free Eppendorf tube containing 60  $\mu\text{L}$  of PBS buffer, and spinning down with a tabletop centrifuge for  $\sim 30$  s. The sample extracted sample was then washed twice to remove the surplus corona motifs by first diluting in PBS to the total volume of 120  $\mu\text{L}$ , followed by centrifugation at 420  $g$  for 30 min and supernatant replacement with fresh PBS buffer (90  $\mu\text{L}$ ). Washed aggregates were pipetted into silicone rubber incubation chambers (6.5 mm  $\times$  6.5 mm  $\times$  3.5 mm, Grace Biolabs FlexWells) and sealed with DNase free tape (Grace Biolabs FlexWell Seal Strips) to prevent evaporation. For imaging, an Ar-ion laser line at 488 nm and an HeNe line at 633 nm were used for excitation of fluorescein (core motifs) and Alexa Fluor 647 (outer corona motifs) dyes, respectively.

### Assessment of i-motif formation with UV absorbance

UV-Vis spectrophotometry was used to characterise i-motif formation (Fig. 2d). Annealed oligonucleotide samples (1200  $\mu\text{L}$ ) in PBM9 medium with pre-adjusted pH were loaded into quartz cuvettes, and their absorbance at 297 nm [57, 58] was measured at room temperature using the aforementioned UV-Vis spectrophotometer. The tested pH ranged from 8 to 4 with steps of 0.25 points. The transitional pH values ( $\text{pK}_A$ ) were calculated with a tailor-made Matlab script as the inflection point of

sigmoidal fits to the experimental data.

### Assessment of i-motif formation with DLS

DLS measurements, performed on the Malvern Zetasizer Nano ZSP setup, were used to confirm the accurateness of the transitional pH value extracted from UV response curves (Fig. 2d). The recorded pH-response curve is shown in Supplementary Fig. 4. For these experiments, 120  $\mu\text{L}$  of the samples containing core and inner corona motifs in PBM9 medium with pre-adjusted pH were pipetted into an ultra-low volume quartz cuvette. Three measurements, each consisting of fifteen data runs, were then taken at room temperature. The tested pH ranged from 8 to 4 with steps of 0.25 points. The plotted  $D_H$  values were extracted from raw intensity profiles using the previously mentioned Matlab script.

### Assessment of i-motif formation with circular dichroism

CD measurements, performed on a JASCO J-810 CD spectrophotometer, were used to further validate the i-motif formation upon pH decrease (Fig. 2e). First, 200  $\mu\text{L}$  of highly concentrated (20  $\mu\text{M}$ ) samples in PBM9 medium with pH adjusted to 7.00 or 4.50 were pipetted into a 1 mm path-length, stoppered quartz cuvette. CD spectra were then acquired at room temperature in the spectral range of 210-350 nm.

### pH-triggered particle aggregation assay with epifluorescence and differential dynamic microscopy

Differential dynamic microscopy (DDM) and epifluorescence microscopy were used to assess the pH-responsiveness of the DNA particles (Fig. 2g and Supplementary Fig. 5). Responsive (two samples) and nonresponsive (one sample) particles prepared in PBS buffer with the thermal annealing protocol described above ( $t_g = 900$  s) were transferred into silicon incubation chambers and supplemented with PB(2 $\times$ )M9 at 1:1 ratio to the final volume of 120  $\mu\text{L}$ . The pH of two of the samples was then adjusted with HCl and KOH to 4.50 before sealing the wells with DNase free tape and imaging for 960 min at 30 min intervals. The remaining sample with responsive particles served as a control. Both high frame-rate bright field videos (150 fps, 8 s) and epifluorescence micrographs were recorded with a fully motorised Nikon Eclipse Ti-E inverted epifluorescence microscope, equipped with CFI

1 Plan Apochromat  $\lambda$  40 $\times$ /0.95 NA dry objective (Nikon),  
2 Grasshopper3 GS3-U3-23S6M camera (Point Gray Re-  
3 search) and Perfect Focusing System (Nikon). For the  
4 epifluorescence imaging of core motifs labelled with Alexa  
5 Fluor 594, red LED illumination and a Texas Red filter  
6 cube (Semrock) were used.  
7 Bright field videos were analysed with DDM [59, 60] us-  
8 ing a custom script written in Matlab, as described in  
9 ref. [54].  
10 Briefly, an image structure function,  $\Delta I(q, \tau)$ , was ob-  
11 tained as

$$\Delta I(q, \tau) = \langle |d(q, t_0, \tau)|^2 \rangle_{t_0}. \quad (1)$$

13 In Eq. 1,  $q$  is the wave-vector in Fourier space  
14 and  $d(q, t_0, \tau)$  is the 2D spatial Fourier transform of  
15  $d(r, t_0, \tau) = I(r, t_0 + \tau) - I(r, t_0)$ , where  $I(r, t_0)$  and  
16  $I(r, t_0 + \tau)$  are two video frames collected at times  $t_0$   
17 and  $t_0 + \tau$ .  $\Delta I(q, \tau)$  was then fitted to [59]

$$\Delta I(q, \tau) = A(q) [1 - \exp(-Dq^2\tau)] + B(q), \quad (2)$$

19 to obtain the Brownian diffusion coefficient  $D$ .  $A(q)$  and  
20  $B(q)$  are functions dependent on the static scattering  
21 properties of the sample, instruments optics and camera  
22 noise.

23 The computed  $D$  was used to calculate the hydrody-  
24 namic radius  $R_H$  from the Stokes-Einstein equation.  
25 Note that at late times, once aggregates become too  
26 large to diffuse and/or start percolating, the extracted  
27  $R_H$  loses its physical meaning. Despite this, all experi-  
28 mental data were fitted to Eq. 2 for consistency.

29 Analysis of epifluorescence micrographs was performed  
30 with a tailor-made Matlab script by calculating the sum  
31 of the background-subtracted pixel intensity within the  
32 observed field of view.

### 34 Particle stability in bacterial growth media

35 DDM was used to evaluate the stability of DNA  
36 particles after deployment in several types of commonly  
37 used bacterial growth media (Supplementary Fig. 6).  
38 Small volumes (60  $\mu$ L) of nonresponsive particles  
39 prepared in PBS buffer using the thermal annealing  
40 protocol described above ( $t_g = 600$  s) were transferred  
41 into three silicon incubation chambers. The wells  
42 were then sealed with DNase free tape and imaged  
43 by recording three high frame-rate bright field videos  
44 (150 fps, 8 s) per sample with the previously described  
45 Nikon Eclipse Ti-E inverted epifluorescence microscope.  
46 After 5 min, the chambers were supplemented with M9  
47 medium (12.8 g L<sup>-1</sup> Na<sub>2</sub>HPO<sub>4</sub> 7H<sub>2</sub>O, 3 g L<sup>-1</sup> KH<sub>2</sub>PO<sub>4</sub>,  
48 0.5 g L<sup>-1</sup> NaCl, 1 g L<sup>-1</sup> NH<sub>4</sub>Cl, 11 mg L<sup>-1</sup> CaCl<sub>2</sub>, 240  
49 mg L<sup>-1</sup> MgSO<sub>4</sub> and 0.4% w/v Glucose), M63 medium  
50 (13.6 g L<sup>-1</sup> KH<sub>2</sub>PO<sub>4</sub>, 0.5 mg L<sup>-1</sup> FeSO<sub>4</sub> 7H<sub>2</sub>O, 0.5

g L<sup>-1</sup> MgSO<sub>4</sub> 7H<sub>2</sub>O, 1.27 mg L<sup>-1</sup> Thiamine, 2.64 g L<sup>-1</sup>  
(NH<sub>4</sub>)<sub>2</sub>SO<sub>4</sub> and 0.5% w/v Glucose) or M63 medium  
containing casamino acids (CAAs, 0.4% w/v) at 1:1  
ratio to the final volume of 120  $\mu$ L. After this, the wells  
were resealed and the samples were imaged by acquiring  
three high frame-rate bright field videos per chamber  
at times  $t = 60, 120, 180, 300$  and 1200 min from the  
growth medium addition.

The acquired data was analysed using a custom DDM  
analysis script written in Matlab, as described in the  
previous section.

### Bacterial strains and growth conditions

All the experiments involving bacteria were carried  
out with the highly motile MG1655 *Escherichia coli*  
strain. For fluorescence imaging (Figs 3d, 4c and  
Supplementary Figs 10, 16), the strain was transformed  
with the pWR20-EGFP plasmid that enables the con-  
stitutive expression of the enhanced green fluorescent  
protein (EGFP) in the cytoplasm and kanamycin resis-  
tance [79, 80].

*E. coli* cells were grown from single colonies in 50  
ml conical glass flask filled with 5 mL of LB medium  
(10 g L<sup>-1</sup> Tryptone, 5 g L<sup>-1</sup> Yeast extract, 0.5 g L<sup>-1</sup>  
NaCl) in an overnight incubation carried out at 37°C,  
with continuous shaking at 220 rpm. A small volume  
(50  $\mu$ L) of the culture in LB was then transferred into  
a glass flask containing 50  $\mu$ L of M63 medium and the  
cells were allowed to grow to an optical 0.2-0.3 OD using  
the same incubation conditions. Before the experiments,  
bacteria were pelleted through centrifugation at 8000  
 $g$  for 2 min, washed twice with fresh buffer (PBS or  
PB(2 $\times$ )M9) and concentrated to obtain a final OD of  
0.11 after dilution by mixing all the components required  
to perform specific experiments. Note that to guarantee  
the expression of EGFP in all *E. coli*, both LB and M63  
media were supplemented with kanamycin.

### PBM9 medium

The deployment of core-shell DNA particles in bac-  
terial cultures yields solutions that are partly made up  
of PBS buffer used in their production. To robustly  
grow bacteria in a medium that matches the ionic  
and buffering characteristics of PBS buffer, we devised  
PBM9 (137 mM NaCl, 2.7 mM KCl, 8 mM Na<sub>2</sub>HPO<sub>4</sub>,  
2 mM KH<sub>2</sub>PO<sub>4</sub>, 18.7 mM NH<sub>4</sub>Cl, 0.1 mM CaCl<sub>2</sub>, 2  
mM MgSO<sub>4</sub>, 0.2% w/v CAAs, various concentrations of  
glucose, pH adjusted to 7.00 with HCl and KOH) which  
is based on the common M9 medium, with the buffering  
and ionic components of PBS.

The medium was used in all the experiments included in this study that involve *E. coli* and/or DNA particles/nanostructures.

### Bacterial growth and pH changes in PBM9 medium

*OD* measurements, performed on the aforementioned UV-Vis spectrophotometer, were used to characterise the bacterial growth in PBM9 medium (Fig. 3b). The accompanying pH changes were tracked using a bench-top pH meter. 250  $\mu\text{L}$  of *E. coli* cells in LB (overnight growth) were loaded into 250 ml conical glass flasks with 24.75 mL of PBM9 medium (various glucose concentrations) and then incubated at 37°C with continuous shaking at 220 rpm. Every 45 minutes, two volumes of 1 ml each were transferred into 1.5 ml Eppendorf tubes. The first sample was pipetted into a disposable cuvette (polystyrene, BRAND) and used to measure *OD*. After the measurement, the aliquot was transferred back into the flask. The second sample was filtered using a 0.22  $\mu\text{m}$  polyethersulfone filter into 50 ml centrifuge tube to remove bacteria cells. The resultant solution was used to measure pH. The procedure described above was repeated eleven times at  $t = 45, 90, 135, 180, 225, 270, 315, 360, 405, 450$  and 495 min, after which the samples were left incubating for additional 960 min with the final measurement performed at the end of incubation cycle.

### Plate reader-based assay of pH and optical density changes accompanying the bacterial growth

Turbidity and fluorescence measurements, performed on a FLUOstar Omega plate reader, were used to determine the optimal glucose concentration enabling bacteria-induced particle activation in conditions used for further experiments (Supplementary Figs 7, 8). *E. coli* cells were initially grown and washed as described above, then resuspended in PBS and loaded into a DNase free, flat-bottom 96-well plate (CELLSTAR Black 96 Well Cell Culture Microplates, Greiner Bio-One). Each well was then topped with 120  $\mu\text{L}$  of PB(2 $\times$ )M9 (various glucose concentration) and 10  $\mu\text{L}$  of fluorescein (FITC)-dextran (3 kDa, anionic, Sigma-Aldrich) solution in PBS to a total volume of 240  $\mu\text{L}$ , resulting in the final FITC-dextran concentration of 50  $\mu\text{M}$  and OD of 0.11. OD and fluorescence intensity at 520 nm upon excitation at 400 nm ( $I_{400}$ ) and 485 nm ( $I_{485}$ ) were measured in the plate reader for 2160 min at 8 min intervals while shaking at 700 rpm in double-orbital mode and keeping the temperature at 37°C. The pH was extracted from the intensity ratio  $I_{485}/I_{400}$  [81] using a calibration curve (Supple-

mentary Fig. 9), The calibration curve was acquired by first preparing 1 mL solutions of 50  $\mu\text{M}$  FITC-dextran in PBM9 (various pH), loading 240  $\mu\text{L}$  of each sample into a 96-well plate, and then measuring  $I_{400}$  and  $I_{485}$  on the plate reader at 37°C. The pH ranged from 8 to 4 at 0.25 intervals, and was adjusted with HCl and KOH. The collected data were processed with a tailor-made Matlab script by fitting with a sigmoid function.

### Bacteria immobilisation assay

For experiments on bacteria-induced particle aggregation and subsequent *E. coli* immobilisation (Figs 3d, e and Supplementary Fig. 11), three wells in a 96-well plate were filled with 10  $\mu\text{L}$  of highly concentrated *E. coli* solution in PBS ( $OD = 0.66$  after 4 $\times$  dilution), prepared as described above, 10  $\mu\text{L}$  of PBS and 120  $\mu\text{L}$  of PB(2 $\times$ )M9 (glucose concentration set at 0.100% w/v or 0.175% w/v after dilution at 1:1 ratio). Two of the wells with different glucose content were topped with 100  $\mu\text{L}$  of the PBS solution containing pH-responsive particles ( $t_g = 15$  s), while the third well was filled with an identical volume of PBS, and used as a control. Afterwards, samples were incubated in the previously introduced plate reader for  $t = 0, 60, 120, 180, 240, 300, 360, 420, 480, 540, 720, 900, 1080, 1260$  and 1440 min at 37°C, with shaking at 500 rpm for 30 s every 5 min. Note that a distinct set of samples was used for each time point.

All samples were imaged with the aforementioned bright field and epifluorescence microscopy setup by taking a set of seven high frame-rate videos (150 fps, 8 s) and epifluorescence micrographs. Green LED illumination/Texas Red filter (Semrock) and blue LED/GFP filter (Semrock) were used to record signals from core motifs (Alexa Fluor 594) and *E. coli* (EGFP), respectively.

The parameter  $\sigma$ , introduced in ref. [54] and used here to gauge bacterial motility (Fig. 3d and Supplementary Fig. 11), was calculated with a custom Matlab script from bright field videos as  $\sigma = \left\langle \sqrt{\frac{\sum_{m=-3}^3 [I(n+m) - \bar{I}]^2}{7}} \right\rangle_n \frac{\sigma_{max}}{7}$ , where  $I(n)$  represents

the  $n$ -th frame of video,  $\bar{I} = \frac{\sum_{m=-3}^3 I(n+m)}{7}$ ,  $\langle \dots \rangle_n$  indicates a rolling average over the entire video, and  $\sigma_{max}$  is the highest intensity standard deviation value recorded in all the videos. Parameter  $\bar{\sigma}$  shown in Fig. 3e was computed by averaging  $\sigma$  over all the pixels in a frame.

Bacterial growth and pH changes occurring throughout the assay (Fig. 3f and Supplementary Fig. 10) were monitored on the plate reader with analogous samples containing non-fluorescent particles and *E. coli* lacking the pWR20-EGFP plasmid. To enable pH tracking, 10  $\mu\text{L}$  of PBS were replaced with an identical volume of 1.2 mM FITC-dextran solution in PBS. Prepared samples were

1 incubated for 1440 min at 37°C with shaking at 500 rpm 51  
2 for 30 s every 5 min.  $OD$ ,  $I_{485}$  and  $I_{400}$  were measured 52  
3 at 5 min intervals over time. The pH was then calcu- 53  
4 lated from  $I_{485}/I_{400}$  using the calibration curve shown in 54  
5 Supplementary Fig. 9. 55

### 6 Bacteria detection with a ratiometric pH probe 58

7 For experiments used to sense pH changes with 59  
8 fluorophore-labelled particles, (Supplementary Fig. 12), 61  
9 two wells in a 96-well plate were filled with 20  $\mu\text{L}$  of 62  
10 PBS solution containing *E. coli* cells ( $OD = 0.66$  before 63  
11 concentrating the cells 2 $\times$ ). Both chambers were then 64  
12 topped with 100  $\mu\text{L}$  of responsive particles ( $t_g = 15$  s) in 65  
13 PBS, which were formed using fluorescein-labelled core 66  
14 motifs, and 120  $\mu\text{L}$  of PB(2 $\times$ )M9 medium with differ- 67  
15 ent glucose concentrations (0.100% w/v or 0.175% w/v 68  
16 in the final solution). Two additional wells were loaded 69  
17 with 240  $\mu\text{L}$  of equimolar particle solutions in PBM9. 70  
18 The pH of one of them was adjusted to 4.50 with HCl 71  
19 and KOH. Fluorescence intensities  $I_{400}$  and  $I_{485}$  were au- 72  
20 tomatically measured in the aforementioned plate reader 73  
21 for 1440 min, at 5 min intervals, temperature set to 37°C, 74  
22 with shaking at 500 rpm for 30 s every 5 min. 75  
23 The recorded fluorescence intensity ratios  $I_{485}/I_{400}$  were 76  
24 used to calculate pH using calibration curve recorded for 77  
25 fluorescein-dextran probes (Supplementary Fig. 9). The 78  
26 use of this calibration curve is justified by the control 79  
27 experiment in Supplementary Fig. 13. 80

### 28 Bacteria sensing with a fluorophore-quencher pair 81

29 Fluorescence measurements used to sense bacteria- 82  
30 induced pH changes with particles modified with the 83  
31 fluorophore-quencher pair (Supplementary Fig. 14) were 84  
32 carried out on the plate reader described above. Rho- 85  
33 damine 6G (Rh6G) and Black Hole Quencher 1 (BHQ1) 86  
34 were used as fluorophore and quencher, respectively. 87  
35 First, small volumes (10  $\mu\text{L}$ ) of *E. coli* solution in PBS 88  
36 (4 $\times$  dilution results in OD of 0.66), prepared as in the 89  
37 protocol described above, were loaded into four wells of 90  
38 a 96-well plate. Two of the chambers were then filled 91  
39 with 100  $\mu\text{L}$  of responsive particles ( $t_g = 15$  s, Rh6G and 92  
40 BHQ1) in PBS, 10  $\mu\text{L}$  of *IM\*-3m* (BHQ1) strand in PBS, 93  
41 and 120  $\mu\text{L}$  of PB(2 $\times$ )M9 medium. The BHQ1-modified 94  
42 strand was included to block any remaining sites with 95  
43 the Rh6G dye located within the particles' cores, that 96  
44 could not be accessed and quenched by inner corona mo- 97  
45 tifs during particle assembly. The two remaining wells 98  
46 were topped with 110  $\mu\text{L}$  of PBS buffer and 120  $\mu\text{L}$  of 99  
47 PB(2 $\times$ )M9 medium. The overall glucose concentration 100  
48 was set to 0.100% w/v or 0.175% w/v and varied between  
49 samples of the same type. In the next step, a control  
50 sample was prepared in a separate well by mixing 100

$\mu\text{L}$  of PBS solution containing responsive particles ( $t_g =$   
15 s, Rh6G) with 20  $\mu\text{L}$  of PBS buffer and 120  $\mu\text{L}$  of  
PB(2 $\times$ )M9 medium. All the samples were incubated in  
the plate reader for 1440 min at 37°C, with shaking at  
500 rpm for 30 s every 5 min. Fluorescence intensity at  
530 nm upon excitation at 485 nm was monitored over  
time every 5 min.

The final curves representing the samples that contain  
both *E. coli* and particles in PBM9 medium with distinct  
glucose concentration, shown in Supplementary Fig. 14,  
were obtained by subtracting the signal recorded from  
analogous samples lacking the particles. This operation  
was performed to eliminate contributions from *E. coli*  
autofluorescence, which can be detected at this wave-  
length [82].

### MIC estimation assay

The minimum inhibitory concentration (MIC) of the  
antibiotic ciprofloxacin was measured using the broth  
microdilution technique [83] on the aforementioned plate  
reader (Supplementary Fig. 15).

Cells were grown in LB at 37°C overnight with shaking  
at 220 rpm, and inoculated at a 1:100 dilution into  
a 96-well plate containing various concentrations of  
ciprofloxacin in PBM9, for a final volume of 200  $\mu\text{L}$ . The  
plate was incubated for 960 min at 37°C with 700 rpm  
shaking in double-orbital mode. OD was monitored over  
time every 13 min.

### Preparation of antibiotic-loaded GUVs

Giant unilamellar vesicles (GUVs) with encapsulated  
ciprofloxacin were prepared using the emulsion-transfer  
method [47, 54, 84].

A glass vial (1.5 mL) was loaded with 500  $\mu\text{L}$  of paraffin  
oil (Sigma-Aldrich) and 100  $\mu\text{L}$  of a 10 mg mL<sup>-1</sup> so-  
lution of 1,2-dioleoyl-sn-glycero-3-phosphocholine lipids  
(DOPC, Avanti Polar Lipids) in chloroform. Afterwards,  
the solution was vortexed for 1 min, incubated for 60  
min at ~85°C to evaporate chloroform, and left for 15  
min to cool down to room temperature. In the next step,  
250  $\mu\text{L}$  of the lipid-oil solution (final lipid concentration  
2 mg mL<sup>-1</sup>) were pipetted into a clean 1.5 mL glass vial  
and mixed with 25  $\mu\text{L}$  of the Inside-solution (I-solution,  
3.2  $\mu\text{g}$  mL<sup>-1</sup> ciprofloxacin and 100  $\mu\text{M}$  dextran (50 kDa,  
Sigma-Aldrich) in PBM9 (glucose replaced with 0.333%  
w/v sucrose)) by vortexing for ~1 min. The generated  
turbid emulsion was layered on top of 150  $\mu\text{L}$  of the  
Outside-solution (O-solution, PBM9 (0.175% w/v  
glucose)) in a 1.5 mL DNase free Eppendorf tube, and  
centrifuged at 9000 *g* for 30 min. After centrifugation,  
first the oil and then the supernatant were removed

1 from the sample, leaving 50  $\mu\text{L}$  of O-solution containing 50  
2 pelleted GUVs. In the final step, the resulting solution  
3 was diluted and resuspended by adding 100  $\mu\text{L}$  of fresh 51  
4 O-solution and gently pipetting it up and down 7-10 52  
5 times. 53  
6

### 7 **Assessment of antimicrobial responses in synthetic** 8 **cell signalling network interfaced with bacteria**

9 To test the response of the full netosis-like pathway 60  
10 (Figs 4b, c and Supplementary Fig. 16), four wells in a 61  
11 96-well plate were loaded with 10  $\mu\text{L}$  of *E. coli* solution 62  
12 in PB(2 $\times$ )M9 ( $OD = 0.66$  before concentrating the cells  
13 4 $\times$ ), prepared according to the aforementioned protocol,  
14 and 90  $\mu\text{L}$  of PB(2 $\times$ )M9. All the wells were then topped 63  
15 with 100  $\mu\text{L}$  of PBS solution containing responsive or  
16 nonresponsive particles ( $t_g = 15$  s, two wells with each  
17 particle type). Finally, 40  $\mu\text{L}$  of ciprofloxacin-loaded 64  
18 GUVs in PBM9 were added to two wells, each carrying  
19 different particle type, while the remaining two wells  
20 were filled with an identical volume of PBM9. The  
21 overall glucose concentration in all the samples was 65  
22 0.175% w/v. Prepared samples were incubated in the 66  
23 plate reader described above for 1440 min at 37°C, 67  
24 with shaking at 500 rpm for 30 s every 5 min. OD was 68  
25 measured at 5 min intervals over time. 69  
26 Prior to, and after incubation, all the samples were  
27 imaged with the aforementioned bright field and epiflu- 70  
28 orescence microscopy setup. Signals from core motifs 71  
29 (Alexa Fluor 594) and *E. coli* (EGFP) were recorded 72  
30 using green LED illumination/Texas Red filter and blue 73  
31 LED/GFP filter, respectively. 74  
32

### 33 **ACKNOWLEDGMENTS**

34 MW acknowledges support from the Engineering 84  
35 and Physical Sciences Research Council (EPSRC), the 85  
36 Department of Physics at the University of Cambridge 86  
37 (McLatchie Trust fund), and the Cambridge Philosoph- 87  
38 ical Society. LDM acknowledges funding from a Royal 88  
39 Society University Research Fellowship (UF160152, 89  
40 URF\R\221009) and from the European Research 90  
41 Council (ERC) under the Horizon 2020 Research 91  
42 and Innovation Programme (ERC-STG No 851667 - 92  
43 NANOCELL). LM, JK and PC acknowledge the UKRI 93  
44 grant EP/T002778/1. FR acknowledges funding from 94  
45 the Leverhulme Trust (EP/S023518/1). The authors 95  
46 thank Zoe Waller for useful discussions. A dataset 96  
47 underpinning these results is freely available at DOI: 97  
48 10.17863/CAM.95810. 98  
49 100  
50

### **AUTHOR CONTRIBUTIONS**

MW designed the DNA sequences. MW and LM de-  
veloped the experimental protocols. JK designed and  
manufactured the setup for efficient fabrication of core-  
shell particles. MW conducted all the experiments apart  
from CD of pH-responsive/nonresponsive DNA struc-  
tures (FR), OD and pH measurements during bacterial  
growth in PBM9 medium (LM, JX), and ciprofloxacin  
MIC in *E. coli* measurement (LM), supported by LM.  
MW analyzed all the data. MW and LDM wrote the  
paper. MW, LM and LDM designed the research. LDM  
supervised the research, aided by PC. All authors dis-  
cussed the results and edited the paper.

### **COMPETING INTERESTS**

The authors declare no competing interests.

\* ld389@cam.ac.uk

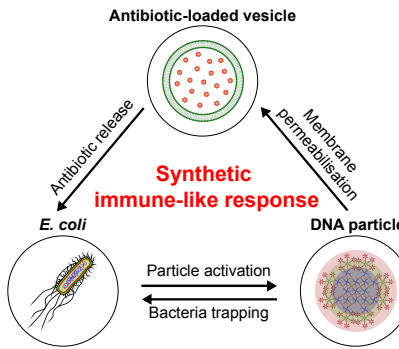
- [1] Blain, J. C. & Szostak, J. W. Progress toward synthetic cells. *Annu. Rev. Biochem.* **83**, 615–640 (2014).
- [2] Buddingh', B. C. & van Hest, J. C. M. Artificial Cells: Synthetic Compartments with Life-like Functionality and Adaptivity. *Accounts of Chemical Research* **50**, 769–777 (2017).
- [3] Cho, E. & Lu, Y. Compartmentalizing cell-free systems: Toward creating life-like artificial cells and beyond. *ACS Synth. Biol.* **9**(11), 2881–2901 (2020).
- [4] Zhu, Y., Guo, X., Liu, J., Li, F. & Yang, D. Emerging advances of cell-free systems toward artificial cells. *Small Methods* **4**(10), 2000406 (2020).
- [5] Boyd, M. A. & Kamat, N. P. Designing artificial cells towards a new generation of biosensors. *Trends Biotechnol.* **39**(9), 927–939 (2021).
- [6] Robinson, A. O., Venero, O. M. & Adamala, K. P. Toward synthetic life: Biomimetic synthetic cell communication. *Curr. Opin. Chem. Biol.* **64**, 165–173 (2021).
- [7] Slomovic, S., Pardee, K. & Collins, J. J. Synthetic biology devices for in vitro and in vivo diagnostics. *Proc. Natl. Acad. Sci. U.S.A.* **112**(47), 14429–14435 (2015).
- [8] Chen, Z. *et al.* Synthetic beta cells for fusion-mediated dynamic insulin secretion. *Nat. Chem. Biol.* **14**, 86–93 (2018).
- [9] Krinsky, N. *et al.* Synthetic cells synthesize therapeutic proteins inside tumors. *Adv. Healthc. Mater.* **7**(1701163) (2018).
- [10] Ding, Y., Contreras-Llano, L. E., Morris, E., Mao, M. & Tan, C. Minimizing context dependency of gene networks using artificial cells. *ACS Appl. Mater. Interfaces* **10**(36), 30137–30146 (2018).
- [11] Toparlak, O. D. *et al.* Artificial cells drive neural differentiation. *Sci. Adv.* **6**(38) (2020).
- [12] Salehi-Reyhani, A., Ces, O. & Elani, Y. Artificial cell mimics as simplified models for the study of cell biology. *Exp. Biol. Med.* **242**(13), 1309–1317 (2017).

- [13] Xu, C., Hu, S. & Chen, X. Artificial cells: from basic science to applications. *Mater. Today* **19(9)**, 516–532 (2016).
- [14] Zhu, T. F. & Szostak, J. W. Coupled growth and division of model protocell membranes. *J. Am. Chem. Soc.* **131(15)**, 5705–5713 (2009).
- [15] Kretschmer, S., Ganzinger, K. A., Franquelim, H. G. & Schwille, P. Synthetic cell division via membrane-transforming molecular assemblies. *BMC Biol.* **17(43)** (2019).
- [16] Steinkühler, J. *et al.* Controlled division of cell-sized vesicles by low densities of membrane-bound proteins. *Nat. Commun.* **11(905)** (2020).
- [17] Lee, K. Y. *et al.* Photosynthetic artificial organelles sustain and control ATP-dependent reactions in a protocellular system. *Nat. Biotechnol.* **36**, 530–535 (2018).
- [18] Berhanu, S., Ueda, T. & Kuruma, Y. Artificial photosynthetic cell producing energy for protein synthesis. *Nat. Commun.* **10(1325)** (2019).
- [19] Deshpande, S., Wunnava, S., Hueting, D. & Dekker, C. Membrane tension-mediated growth of liposomes. *Small* **15(38)**, 1902898 (2019).
- [20] Downs, F. G. *et al.* Multi-responsive hydrogel structures from patterned droplet networks. *Nat. Chem.* **12**, 363–371 (2020).
- [21] Zhang, S. *et al.* Engineering motile aqueous phase-separated droplets via liposome stabilisation. *Nat. Commun.* **12(1673)** (2021).
- [22] Mukwaya, V., Mann, S. & Dou, H. Chemical communication at the synthetic cell/living cell interface. *Commun. Chem.* **4(161)** (2021).
- [23] Smith, J. M., Chowdhry, R. & Booth, M. J. Controlling synthetic cell-cell communication. *Front. Mol. Biosci.* **8(809945)** (2022).
- [24] Garamella, J., Majumder, S., Liu, A. P. & Noireaux, V. An adaptive synthetic cell based on mechanosensing, biosensing, and inducible gene circuits. *ACS Synth. Biol.* **8(8)**, 1913–1920 (2019).
- [25] Kaufhold, W. T., Brady, R. A., Tuffnell, J. M., Cicuta, P. & Di Michele, L. Membrane Scaffolds Enhance the Responsiveness and Stability of DNA-Based Sensing Circuits. *Bioconjug. Chem.* (2019).
- [26] Samanta, A., Sabatino, V., Ward, T. R. & Walther, A. Functional and morphological adaptation in DNA protocells via signal processing prompted by artificial metalloenzymes. *Nat. Nanotechnol.* **15**, 914–921 (2020).
- [27] Leathers, A. *et al.* Reaction-diffusion patterning of DNA-based artificial cells. *J. Am. Chem. Soc.* **144(38)**, 17468–17476 (2022).
- [28] Rubio-Sánchez, R., Barker, S. E., Walczak, M., Cicuta, P. & Di Michele, L. A Modular, Dynamic, DNA-Based Platform for Regulating Cargo Distribution and Transport between Lipid Domains. *Nano Lett.* **21**, 2800–2808 (2021).
- [29] Elani, Y., Law, R. V. & Ces, O. Protein synthesis in artificial cells: using compartmentalisation for spatial organisation in vesicle bioreactor. *Phys. Chem. Chem. Phys.* **17**, 15534–15537 (2015).
- [30] van Nies, P. *et al.* Self-replication of DNA by its encoded proteins in liposome-based synthetic cells. *Nat. Commun.* **9(1583)** (2018).
- [31] Rideau, E., Dimova, R., Schwille, P., Wurm, F. R. & Landfeste, K. Liposomes and polymersomes: a comparative review towards cell mimicking. *Chem. Soc. Rev.* **47**, 1283–1292 (2018).
- [32] Stano, P. Gene expression inside liposomes: From early studies to current protocols. *Chem. Eur. J.* **25(33)**, 7798–7814 (2019).
- [33] Niederholtmeyer, H., Chaggan, C. & Devaraj, N. K. Communication and quorum sensing in non-living mimics of eukaryotic cells. *Nat. Commun.* **9(5027)** (2018).
- [34] Huang, X. *et al.* Interfacial assembly of protein-polymer nano-conjugates into stimulus-responsive biomimetic protocells. *Nat. Commun.* **4(2239)** (2013).
- [35] Joesaar, A. *et al.* DNA-based communication in populations of synthetic protocells. *Nat. Nanotechnol.* **14**, 369–378 (2019).
- [36] Mason, A. F. & van Hest, J. C. M. Multifaceted cell mimicry in coacervate-based synthetic cells. *Emerg. Top. Life Sci.* **3(5)**, 567–571 (2019).
- [37] Allen, M. E., Hindley, J. W., Baxani, D. K., Ces, O. & Elani, Y. Hydrogels as functional components in artificial cell systems. *Nat. Rev. Chem.* **6**, 562–578 (2022).
- [38] Xu, C., Martin, N., Li, M. & Mann, S. Living material assembly of bacteriogenic protocells. *Nature* **609**, 1029–1037 (2022).
- [39] Rubio-Sánchez, R., Fabrini, G., Cicuta, P. & Di Michele, L. Amphiphilic DNA nanostructures for bottom-up synthetic biology. *Chem. Commun.* **57**, 12725–127405 (2021).
- [40] Marshall, J. S., Warrington, R., Watson, W. & Kim, H. L. An introduction to immunology and immunopathology. *Allergy Asthma Clin. Immunol.* **14(49)** (2018).
- [41] Diamond, M. S. & Kanneganti, T. Innate immunity: the first line of defense against SARS-CoV-2. *Nat. Immunol.* **23**, 165–176 (2022).
- [42] Lim, B. *et al.* Reprogramming synthetic cells for targeted cancer therapy. *ACS Synth. Biol.* **11(3)**, 1349–1360 (2022).
- [43] Gardner, P. M., Winzer, K. & Davis, B. G. Sugar synthesis in a protocellular model leads to a cell signalling response in bacteria. *Nat. Chem.* **1**, 377–383 (2009).
- [44] Lentini, R. *et al.* Integrating artificial with natural cells to translate chemical messages that direct *E. coli* behaviour. *Nat. Commun.* **5(4012)** (2014).
- [45] Schwarz-Schilling, M., Aufinger, L., Mückl, A. & Simmel, F. C. Chemical communication between bacteria and cell-free gene expression systems within linear chains of emulsion droplets. *Integr. Biol.* **8(4)**, 564–570 (2016).
- [46] Lentini, R. *et al.* Two-way chemical communication between artificial and natural cells. *ACS Cent. Sci.* **3(2)**, 117–123 (2017).
- [47] Rampioni, G. *et al.* Synthetic cells produce a quorum sensing chemical signal perceived by *Pseudomonas aeruginosa*. *Chem. Commun.* **54**, 2090–2093 (2018).
- [48] Wang, X. *et al.* Chemical communication in spatially organized protocell colonies and protocell/living cell microarrays. *Chem. Sci.* **10(41)**, 9446–9453 (2019).
- [49] Smith, J. M., Hartmann, D. & Booth, M. J. Engineering cellular communication between light-activated synthetic cells and bacteria. *bioRxiv* (2022).
- [50] Gispert, I. *et al.* Stimuli-responsive vesicles as distributed artificial organelles for bacterial activation. *Proceedings of the National Academy of Sciences* **119(42)**, e2206563119 (2022).
- [51] Brinkmann, V. *et al.* Neutrophil extracellular traps kill bacteria. *Science* **303(5663)**, 1532–1535 (2004).



- [52] Kaplan, M. J. & Radic, M. Neutrophil extracellular traps: double-edged swords of innate immunity. *J. Immunol.* **189**(6), 2689–2695 (2012).
- [53] Papayannopoulos, V. Neutrophil extracellular traps in immunity and disease. *Nat. Rev. Immunol.* **18**, 134–147 (2018).
- [54] Walczak, M. *et al.* Responsive core-shell DNA particles trigger lipid-membrane disruption and bacteria entrapment. *Nat. Commun.* **12**(4743) (2021).
- [55] Sánchez-Clemente, R. *et al.* Study of pH changes in media during bacterial growth of several environmental strains. *Proceedings* **2**(20), 1297 (2018).
- [56] Shu, W. *et al.* DNA molecular motor driven micromechanical cantilever arrays. *J. Am. Chem. Soc.* **127**(48), 17054–17060 (2005).
- [57] Dvořáková, Z. *et al.* i-motif of cytosine-rich human telomere DNA fragments containing natural base lesions. *Nucleic Acids Res.* **46**(4), 1624–1634 (2018).
- [58] Školáková, P. *et al.* Systematic investigation of sequence requirements for DNA i-motif formation. *Nucleic Acids Res.* **47**(5), 2177–2189 (2019).
- [59] Cerbino, R. & Trappe, V. Differential dynamic microscopy: Probing wave vector dependent dynamics with a microscope. *Phys. Rev. Lett.* **100**(18), 188102 (2008).
- [60] Cerbino, R. & Cicuta, P. Perspective: Differential dynamic microscopy extracts multi-scale activity in complex fluids and biological systems. *J. Chem. Phys.* **147**, 110901 (2017).
- [61] Brady, R. A., Brooks, N. J., Cicuta, P. & Di Michele, L. Crystallization of amphiphilic DNA c-stars. *Nano Lett.* **17**(5), 3276–3281 (2017).
- [62] Brady, R. A., Brooks, N. J., Fodera, V., Cicuta, P. & Di Michele, L. Amphiphilic-DNA platform for the design of crystalline frameworks with programmable structure and functionality. *J. Am. Chem. Soc.* **140**(45), 15384–15392 (2018).
- [63] Brady, R. A., Kaufhold, W. T., Brooks, N. J., Fodera, V. & Di Michele, L. Flexibility defines structure in crystals of amphiphilic DNA nanostars. *J. Phys.: Cond. Matter* **31**, 074003 (2019).
- [64] Nesterova, I. V. & Nesterov, E. E. Rational design of highly responsive pH sensors based on DNA i-motif. *J. Am. Chem. Soc.* **136**(25), 8843–8846 (2014).
- [65] Chen, N. *et al.* Real-time monitoring of dynamic microbial Fe(III) respiration metabolism with a living cell-compatible electron-sensing probe. *Angew. Chem.* **61**(18), e202115572 (2022).
- [66] Wang, L. *et al.* Engineering consortia by polymeric microbial swarmbots. *Nature Communications* **13**, 3879 (2022).
- [67] Balasubramanian, S., Aubin-Tam, M.-E. & Meyer, A. S. 3D printing for the fabrication of biofilm-based functional living materials. *ACS Synthetic Biology* **8**, 1564–1567 (2019).
- [68] Yamashita, T. & Yamamoto-Ikemoto, R. Nitrogen and phosphorus removal from wastewater treatment plant effluent via bacterial sulfate reduction in an anoxic bioreactor packed with wood and iron. *Int. J. Environ. Res. Public Health* **11**(9), 9835–9853 (2014).
- [69] Van Dillewijn, P., Nojiri, H., Van Der Meer, J. R. & Wood, T. K. Bioremediation, a broad perspective. *Microb. Biotechnol.* **2**(2), 125–127 (2009).
- [70] Rodrigo-Navarro, A., Sankaran, S., Dalby, M. J., del Campo, A. & Salmeron-Sanchez, M. Engineered living biomaterials. *Nature Reviews Materials* **6**, 1175–1190 (2021).
- [71] Ming, Z. *et al.* Living bacterial hydrogels for accelerated infected wound healing. *Advanced Science* **8**, 2102545 (2021).
- [72] Bhusari, S., Sankaran, S. & del Campo, A. Regulating bacterial behavior within hydrogels of tunable viscoelasticity. *Advanced Science* **9**, 2106026 (2022).
- [73] Hu, Y. *et al.* Identification of bacterial surface antigens by screening peptide phage libraries using whole bacteria cell-purified antisera. *Front. Microbiol.* **8**(82) (2017).
- [74] Memar, M. Y. & Baghi, H. B. Presepsin: A promising biomarker for the detection of bacterial infections. *Biomed. Pharmacother.* **111**, 649–656 (2019).
- [75] Mognetti, B. M., Cicuta, P. & Di Michele, L. Programmable interactions with biomimetic DNA linkers at fluid membranes and interfaces. *Rep. Prog. Phys.* **82**, 116601 (2019).
- [76] Morzy, D. *et al.* Cations regulate membrane-attachment and functionality of DNA nanostructures. *J. Am. Chem. Soc.* **143**, 7358–7367 (2021).
- [77] Zadeh, J. N. *et al.* NUPACK: analysis and design of nucleic acid systems. *J. Comput. Chem.* **32**, 170–173 (2011).
- [78] Mergny, J. L. & Lacroix, L. Analysis of thermal melting curves. *Oligonucleotides* **13**(6), 515–537 (2003).
- [79] Lord, N. *Fluctuation timescales in bacterial gene expression*. Ph.D. thesis, Harvard University (2014).
- [80] Mancini, L. *et al.* A general workflow for characterization of nernstian dyes and their effects on bacterial physiology. *Biophys. J.* **118**(1), 4–14 (2020).
- [81] Bright, G. R., Fisher, G. W., Rogowska, J. & Taylor, D. L. Fluorescence ratio imaging microscopy: temporal and spatial measurements of cytoplasmic pH. *J. Cell Biol.* **104**(4), 1019–1033 (1987).
- [82] Surre, J. *et al.* Strong increase in the autofluorescence of cells signals struggle for survival. *Sci. Rep.* **8**(12088) (2018).
- [83] Wiegand, I., Hilpert, K. & Hancock, R. E. W. Agar and broth dilution methods to determine the minimal inhibitory concentration (MIC) of antimicrobial substances. *Nat. Protoc.* **3**, 163–175 (2011).
- [84] Fujii, S. *et al.* Liposome display for in vitro selection and evolution of membrane proteins. *Nat. Protoc.* **9**, 1578–1591 (2014).

## Table of Contents



Bottom-up synthetic biology aims to replicate useful biological functions, but mimicking complex behaviours such as immunity remains elusive. Here, a synthetic consortium consisting of DNA particles and lipid vesicles is shown to detect bacteria, trap them, and expose them to antibiotics, imitating a core response of the innate immune system. These results demonstrate the bottom-up design of advanced life-like responses and outline new artificial-cell-based antimicrobial strategies.